Journal of Catalysis 400 (2021) 124–139

Contents lists available at ScienceDirect

Journal of Catalysis

journal homepage: www.elsevier.com/locate/jcat

Comparing alkene-mediated and formaldehyde-mediated diene formation routes in methanol-to-olefins catalysis in MFI and CHA

Lauren Kilburn [1], Mykela DeLuca [1], Alexander J. Hoffman, Shivang Patel, David Hibbitts *

Department of Chemical Engineering, University of Florida, Gainesville, FL 32608, United States

ARTICLE INFO

Article history:
Received 4 February 2021
Revised 22 April 2021
Accepted 7 May 2021
Available online 19 May 2021

Keywords:
Zeolites
Methanol-to-olefins
Deactivation
Hydrocarbon pool
Dienes
Hydride transfer

ABSTRACT

This work uses DFT to investigate diene formation during methanol-to-olefins (MTO) via alkene-mediated and CH_2O-mediated pathways in MFI and CHA zeolites. The rate controlling hydride transfer reactions were investigated with C_1–C_4 surface-bound alkyls present during MTO. In the CH_2O-mediated pathway, rate-determining hydride transfer between surface-bound alkyl and CH_3OH occurs most favorably with *tert*-butyl where rates of the hydride transfer exceed that of methyl at C_4:C_1 alkyl ratios as low as 10^{-10} in MFI and 10^{-6} in CHA. In the alkene-mediated route, hydride transfers proceed most favorably between C_4H_8 and secondary alkyls to form butadiene, where propyl--C_4H_8 (in MFI) and *sec*-butyl--C_4H_8 (in CHA) hydride transfers occur over methyl--C_4H_8 when their relative surface concentrations are 10^{-10} and 10^{-5} times that of methyl, respectively. Generally, once formed, C_{2+} surface alkyls are better hydride acceptors than CH_3–Z, suggesting deactivation may be driven by larger surface-bound alkyls, formed by MTO products.

1. Introduction

Zeolites are microporous aluminosilicate materials with many industrial applications, such as fluid catalytic cracking processes [1–6], and are widely studied academically [7–13]. The substitution of Si^{4+} with Al^{3+} in these frameworks yields a charge imbalance which can be mitigated by a proton (H^+) to form a Brønsted acid site. Methanol-to-olefins (MTO) processes in proton-form zeolites form light olefins through pathways mediated by aromatic cocatalysts occluded within zeolites near internal Brønsted acid sites. Previous computational [14–18] and experimental [19–26] work has demonstrated that CH_3OH and CH_3OCH_3 react with hydrocarbon species in zeolite cavities to produce C_2–C_4 alkenes via a hydrocarbon pool mechanism. Two complementary cycles—olefin and aromatic—cooperate during MTO to selectively form C_2–C_4 alkenes [14,24,27–30]. Olefins are repeatedly methylated to a size capable of cracking (C_{6+}) to form C_3–C_8 alkenes which can egress from the zeolite as products or participate in the olefin cycle [24,31–33]. Alternatively, olefins can undergo hydride transfer reactions to form alkanes and dienes [34–38], which can lead to the formation of aromatics via cyclization reactions [39–41]. These aromatics cocatalyze the formation of alkenes through isomerization reactions in the aromatic cycle.[14,15,32,42,43] Additional cyclization reactions between dienes and aromatic cocatalysts can lead to the formation of polyaromatic coke species [4,44–47], which block access to catalytically active Brønsted acid sites and deactivate the catalyst. Diene species formed during MTO processes are critical in both catalyst activation and deactivation pathways; therefore, a comprehensive understanding of diene formation pathways is crucial for the rational design of MTO catalysts to promote or inhibit such reactions.

Hydrogen transfer reactions, including protonation and hydride transfers, mediate the formation of dienes, arenes, and polyaromatic species [36,48,49]. Hydrogen transfers typically involve a bimolecular reaction between a hydride donor—generally an alkane or alkene—and a hydride acceptor—a surface-bound alkyl or carbenium ion. Measuring the propagation of these reactions typically involves measuring the amount of hydrogen transfer products—alkanes and aromatics—and these products are observed with pure alkene feeds in H-ZSM-5 frameworks. Prior studies have demonstrated direct correlations between arene and alkane selectivities [50,51], suggesting that hydrogen transfer reactions can occur between two alkene species in either a concerted alkene hydride transfer mechanism:

$$C_xH_{2x} + C_yH_{2y} \rightarrow C_xH_{2x+2} + C_yH_{2y-2} \quad (1)$$

or this can happen in a sequential mechanism where the alkene first forms a surface-bound alkyl species

* Corresponding author.
E-mail address: hibbitts@che.ufl.edu (D. Hibbitts).
[1] L.K. and M.D. contributed equally to this work.

https://doi.org/10.1016/j.jcat.2021.05.010
0021-9517/

$$C_xH_{2x} + H{-}Z \rightarrow C_xH_{2x+1}{-}Z \quad (2)$$

and the alkyl species can react with another alkene to form a diene:

$$C_xH_{2x+1}{-}Z + C_yH_{2y} \rightarrow C_xH_{2x+2} + C_yH_{2y-2} + H{-}Z \quad (3)$$

where Z represents the zeolite framework. Kinetic studies examining 1-hexene conversion over H-ZSM-5 demonstrated that pure 1-hexene feeds show ~0.15% selectivity to hydrogen transfer products (0.0297 bar 1-hexene, 723 K, 80% conversion) [48]. These results are corroborated by work investigating hydrogen transfer product yield in pure C_5–C_7 olefin co-feeds which show 0.5% selectivity towards hydrogen transfer products in H-ZSM-5 (0.004 bar alkene, 723 K, 96% conversion, 0.4 min kg_{cat} mol^{-1}) [52].

Selectivity towards hydrogen transfer products increases in methanol-olefin mixed co-feeds [48,49,52], suggesting that methanol can facilitate hydride transfers. Co-feeding methanol with C_5–C_7 olefin co-feeds (0.1 bar CH_3OH, 0.004 bar alkene, 723 K, 96% conversion, 0.4 min kg_{cat} mol^{-1}) increases hydrogen transfer product selectivity up to 2.5% (from 0.5% in pure olefin co-feed) [52]. These studies suggest that methanol can participate in hydrogen transfer reactions and decompose to formaldehyde (CH_2O) and methane (CH_4), the former of which subsequently reacts with an alkene to form dienes. CH_3OH can facilitate hydrogen transfer through a methanol disproportionation route, first involving formation of a CH_3–Z group, which occurs facilely at high temperatures: [53]

$$CH_3OH + H{-}Z \rightarrow H_2O + CH_3{-}Z \quad (4)$$

Surface-bound methyl groups can then react with methanol to form CH_2O and methane, which occurs readily during MTO: [49,54–56]

$$CH_3{-}Z + CH_3OH \rightarrow CH_4 + CH_2O + H{-}Z \quad (5)$$

Formaldehyde can alternatively be formed via a one-step concerted mechanism:

$$CH_3OH + CH_3OH \rightarrow CH_4 + H_2O + CH_2O \quad (6)$$

and can be present as a surface hydroxymethyl group through protonation:

$$CH_2O + H{-}Z \rightarrow CH_2OH{-}Z \quad (7)$$

Formaldehyde or hydroxymethyl can react with an alkene to form an alcohol:

$$CH_2OH{-}Z + C_xH_{2x} \rightarrow C_{x+1}H_{2x+1}OH \quad (8)$$

which can dehydrate to form a diene

$$C_{x+1}H_{2x+1}OH \rightarrow C_{x+1}H_{2x} + H_2O \quad (9)$$

This mechanism has been proposed alongside prior experimental studies [36], but the complete pathway has not been investigated using density functional theory (DFT) in common MTO zeolites.

Kinetic studies have demonstrated that increasing the methanol inlet pressure (0.6–52.5 kPa) results in a monotonic increase in the ethene:propene ratio (2–18) during MTO reactions in H-ZSM-5 (30% conversion, 623–773 K), and this increase is attributed to enhanced propagation of the aromatic cycle at higher methanol pressures [57]. This same study co-fed formaldehyde (1.1×10^{-4} bar) and propene (0.001 bar) and observed 5.5-fold increases in aromatic selectivity, indicating that formaldehyde, once formed, contributes to aromatic formation [57]. Formaldehyde scavenging Y_2O_3 species reduce the rate of deactivation in CHA when co-fed during MTO processes [58], further suggesting that formaldehyde facilitates diene formation and deactivation. Catalyst lifetimes can also be extended by H_2 cofeeds in a variety of topological frameworks, including CHA and MFI [59,60]. Co-feeding H_2 decreases the ethene:propene ratio within H-ZSM-5, likely because elimination of hydrogen poor compounds (dienes and CH_2O) decreases the propagation of the aromatics cycle [59,60]. Experimental results demonstrate that rate constants of butadiene and CH_2O hydrogenation are >15× higher than that of propene [60,61], and this is corroborated by theoretical work suggesting that effective barriers of butadiene, hexadiene, and CH_2O hydrogenation are 10–30 kJ mol^{-1} lower than that of C_2–C_4 alkenes in MFI and CHA [62]. These studies suggest that methanol-derived formaldehyde and dienes are critical to initial aromatic formation and catalyst deactivation.

To our knowledge, there are no rigorous periodic DFT studies comparing hydrogen transfer mechanisms to determine the source of induction and deactivation in MTO processes. Molecular understanding of the steps that govern the rates and relative abundances of these routes can provide valuable insights into the formation of precursors to deactivation. Such an understanding would allow for controlled propagation of the aromatic or alkene cycles during MTO and clarify catalyst deactivation mechanisms.

Here, we compare two possible diene formation pathways—alkene-mediated and CH_2O-mediated—in MFI and CHA zeolites. We elucidate the effects of zeolite topology and kinetics governing these hydrogen transfer reactions to provide insight to the primary route of diene formation. Reactant, transition state, and product structures for each step were optimized and then systematically reoriented to increase the likelihood of identifying global minima and accurate saddle points for each state. Butadiene and CH_2O formation occur via reaction pathways that are governed by the rate of hydride transfer between a surface-bound alkyl and either C_4H_8 (alkene-mediated; C_4H_8 refers specifically to *trans*-2-butene in this work) or CH_3OH (CH_2O-mediated). This critical transition state was investigated with C_1–C_4 alkyls which can either react with C_4H_8 or CH_3OH to form butadiene or CH_2O, respectively. We find that the predominant pathway is primarily dependent on the concentration of surface-bound alkyls and the ratio of gas-phase CH_3OH:C_4H_8. Once the hydrocarbon pool is formed and alkenes (and thus surface-bound alkyls) are present, the two mechanisms proceed most favorably when secondary (C_4H_8 hydride donor) or tertiary (CH_3OH hydride donor) act as hydride acceptors in both frameworks. During MTO, CH_3OH pressure tends to be larger than that of C_4H_8, indicating that CH_2O-mediated pathways likely prevail at relevant conditions. As such, we demonstrate that C_{2+} alkyls, rather than CH_3–Z species formed from reactants (CH_3OH or CH_3OCH_3), are primarily responsible for forming butadiene through direct or indirect (CH_2O) mechanisms during MTO. Although the reactions investigated here are only a subset of those involved in the complex process of catalyst deactivation, our insights regarding formaldehyde formation provide a crucial component to understanding the entire mechanism of deactivation during MTO.

2. Methods

2.1. Computational methods

The Vienna ab initio simulation package (VASP) [63–66] was used to execute DFT calculations in fully periodic CHA and MFI unit cells. All calculations were implemented in the Computational Catalysis Interface (CCI) [67]. Planewaves with an energy cutoff of 400 eV were composed using projector augmented wave (PAW) potentials. Structures were optimized using the Perdew-Burke-Ernzerhof (PBE) exchange-correlation functional [68–70] and the DFT-D3 method with Becke and Johnson damping to adjust for dispersive interactions [71–73]. We note that PBE-D3 functionals are susceptible to large errors in entropy. Structures

were optimized in a two-step process, which is ~3× more efficient than traditional single-step optimizations [67]. No atoms were constrained during optimizations. In the first step, structures were electronically converged such that energies varied by $<10^{-4}$ eV between iterations and until the forces on each atom were <0.05 eV $Å^{-1}$. This electronic convergence criterion results in inaccurate force calculations near potential energy minima, so structures were further optimized such that energies varied by $<10^{-6}$ eV between iterations and until the forces on each atom were <0.05 eV $Å^{-1}$. The Brillouin Zone was sampled at the Γ-point [74].

The MFI structure (Fig. S1) was obtained from the results of van Koningsveld et al. because restructuring artifacts are minimized in this zeolite form [75]. The MFI O-site indices referenced in this work are from the International Zeolite Association (IZA) [76]. The indices are listed along with the van Koningsveld indices and corresponding void environment in Table S4 of the Supplemental Information. The CHA structure (Fig. S2) was acquired from the IZA database [76]. The shape and lattice parameters for CHA (a = b = 13.675 Å, c = 14.7670 Å, α = β = 90.0°, γ = 120.0°) and MFI (a = 20.090 Å, b = 19.738 Å, c = 13.142 Å) were fixed. All calculations in CHA were performed at the single crystallographically unique tetrahedral site (T-site) within the framework, which has four unique O atoms. All calculations in MFI were performed at T11, positioned to provide access to the straight channel and its intersection with the sinusoidal channel. T11 has been previously demonstrated to have lower effective barriers for surface methylation than T3, T10, and T12 in MFI [77]. Furthermore, recent work examining Al siting within MFI has demonstrated that T11 is among the two most favorable Al site locations [78], supporting its selection for analysis in this work. There are four O atoms surrounding T11 of MFI: O14, O16, O24, and O25. However, O24 is largely inaccessible to species the size of methanol and larger [79]. Prior theoretical and experimental work examining acid strength in zeolites has shown that all O-sites within a zeolite have deprotonation energies within 12 kJ mol^{-1}, suggesting acid strength does not significantly vary with O-site location [80,81]. Rather, O-site location effects primarily affect confinement of transition states, thus altering enthalpic and entropic contributions to reaction and activation energies.

The nudged elastic band (NEB) [82] method with 12–16 images was used to initiate transition state searches. NEBs were converged such that the forces on all atoms in each image were <0.5 eV $Å^{-1}$. Transition states were refined using the Dimer method [83] and optimized until the forces converged to 0.05 eV $Å^{-1}$. Dimer calculations were performed using a two-step method similar to that used for optimizations.

A fixed displacement method was used to determine vibrational frequencies for reactant, product, and transition states. Zero-point vibrational energies (ZPVE) and temperature-corrected free energies (G) and enthalpies (H) were subsequently calculated for each state from vibrational frequencies (equations given in Section S2). Similar to prior work [62,77,84], inaccurate low frequency modes (<60 cm^{-1}) were replaced with 60 cm^{-1} with the exception of imaginary modes along reaction coordinates in transition states. All framework atoms were fixed during frequency calculations, except for the adsorbed species, the framework Al atom of the Brønsted acid site, the proton, and the O atoms attached to Al atom. We note that PBE-D3 functionals are susceptible to large errors in entropy; however, these errors are generally consistent across different reactions and catalysts allowing comparison in barriers [85]. Our goal here is to compare relative reaction rates for different pathways, not to accurately predict measured rates, and systematic reorientations (Section 2.2) are used to improve the accuracy of these relative comparisons.

2.2. Reorientations of Reactants, Products, and transition states

All reactant, product, and transition states were initially optimized by DFT from manually generated images that formed only a small subset of all possible structures. To increase the likelihood of determining the global energy minima, all states were systematically reoriented based on their specific interactions with the zeolite framework and each reorientation was re-optimized with the same criteria described in Section 2.1. The interactions between the zeolite framework and adsorbates include electrostatic and dispersive interactions, H-bonding between adsorbates and framework oxygen atoms, and covalent bonding of adsorbed species to the acid site, the latter two of which constitute strong interactions that were kept intact during reorientation. The structures were reoriented spatially if there were no strong interactions between the adsorbate and framework, internally for transition states, and around the acid site for states strongly bound (H-bound or covalently bound) to the acid site. The purpose of these reorientations is to probe the potential energy surface more rigorously, while avoiding costly molecular dynamics simulations. Each reoriented state has 10–100 calculated orientations with an energy range of ~10–50 kJ mol^{-1}. We note that these techniques may not identify the global minima but, as demonstrated by previous work [79], improves the accuracy of energies obtained from DFT optimizations while being ~100× more efficient than AIMD simulations.

3. Results and discussion

3.1. Alkene-mediated pathway in MFI

The alkene-mediated pathway can occur by a single-step concerted mechanism (Eq. (1)), where *trans*-butene (C_4H_8) and ethene (C_2H_4) directly react with each other to form 1,3-butadiene (C_4H_6) and ethane (C_2H_6) (Scheme 1). Alternatively, a two-step sequential mechanism (Eqs. (2) and (3)) can occur where ethene first reacts with a proton to form a surface-bound ethyl (or ethoxide), C_2H_5–Z, which subsequently reacts with butene to form butadiene and ethane (Scheme 1). Rate constants for kinetically relevant steps are defined in Scheme 1 and discussed further at the end of this section. C_2H_4 and C_4H_8 are the two smallest molecules capable of producing butadiene via the alkene-mediated route and are discussed in this section; however, these reactions can occur with a variety of surface-bound alkyls, which are examined in Section 3.5.

The formation of a surface-bound alkyl (e.g., C_2H_5–Z) is the first step of the sequential mechanism and involves the protonation of an alkene with the concurrent formation of a C–O framework bond. Formation of C_2H_5–Z was investigated at all O-site combinations involving O14, O16, and O25 which surround T11 (O24 was neglected because it is geometrically hindered by the framework, causing high transition state barriers) [79]. The most favorable C_2H_5–Z formation transition state occurs between O16 (protonation) and O25 (C–O bond formation), two O-sites that bridge the straight channel and the channel intersection (Fig. 1a). Reactions at O14 within the straight channel are less favorable (by 21 kJ mol^{-1}, Fig. S3), indicating a preference for the straight channel pore mouth. Previous work [62,79] has demonstrated that smaller transition states preferentially sit in straight channel or at the edge of the straight channel and channel intersection where stabilizing, non-covalent interactions with the framework are maximized, and this same trend is observed for all alkyl-formation steps. This reaction occurs with an intrinsic free energy barrier (ΔG_{act}) of 83 kJ mol^{-1} and reaction free energy (ΔG_{rxn}) of −13 kJ mol^{-1} (Fig. 2a), which agrees well with previous computational work in TON suggesting that C_2H_5–Z occurs with a ΔG_{rxn} of −17 kJ mol^{-1} [86].

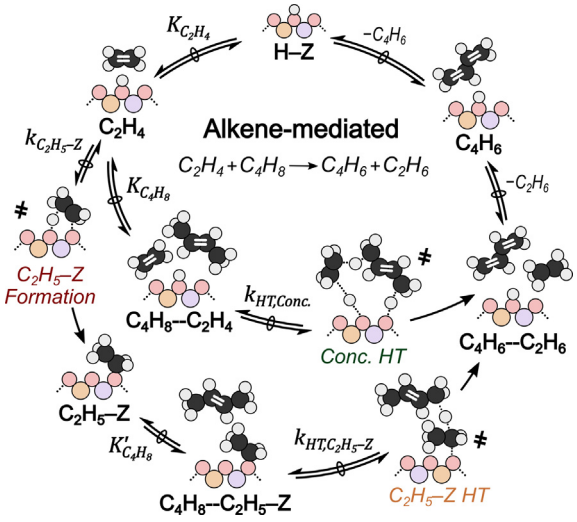

Scheme 1. Concerted and sequential routes of the alkene-mediated pathway with ethene (C_2H_4) as the hydride acceptor and butene (C_4H_8) as the hydride donor. Relevant transition states, C_2H_5–Z formation (red), C_2H_5–Z hydride transfer (HT, orange), and concerted hydrogen transfer (green) are labeled, and associated K and k values (used in Eq. (10) and Section S3) are listed.

Spectating aromatics have been shown to facilitate CH_3–Z formation via CH_3OH dehydration [79], so C_2H_5–Z formation was also investigated with a spectating C_4H_8. The most favorable transition state is positioned at the edge of the straight channel, similar to C_2H_5–Z formation without spectating C_4H_8 (Fig. 1a), but its orientation is now parallel to C_4H_8 (Fig. 1b). This reaction was also examined at all O-site combinations involving T11, and it prefers reacting across the O16-O25 site-pair. The parallel orientation between C_2H_4 and C_4H_8 is also evident in the most favorable O16-O14 and O14-O25 transition states, which are 49 and 43 kJ mol^{-1} less favorable, respectively (Fig. S4). The presence of co-adsorbed C_4H_8, however, does not alter the intrinsic free energy barrier (ΔG_{act} of 83 kJ mol^{-1}, Fig. 1b) compared to the same reaction in the absence of C_4H_8, in contrast to the prior work for methanol dehydration near aromatics [79]. This difference likely arises because C_4H_8 is smaller than benzene and does not offer the same van der Waals stabilization. This inability of C_4H_8 to lower the C_2H_5–Z formation intrinsic barrier along with the entropy-loss associated with the co-adsorption of C_2H_4 and C_4H_8 at a single acid site suggests that this reaction is likely to occur in the absence of co-adsorbed C_4H_8. Notably, this transition state, and those shown in Fig. 1c and d, have negative effective enthalpy barriers relative to a bare acid site (proton). The negative barrier stems from adsorption of C_2H_4 and C_4H_8 being a combined 81 kJ mol^{-1} lower in enthalpy than the reference state of a bare proton (Fig. S39). However, this reference state is not likely representative of the most abundant surface intermediate (MASI) during MTO reactions, and we do not expect these reactions to have negative effective enthalpy barriers if measured experimentally.

The second step of the sequential mechanism is the hydride transfer from C_4H_8 to C_2H_5–Z, and it occurs with a ΔG_{act} of 61 kJ mol^{-1} (Fig. 1c). After the hydride is transferred to C_2H_5–Z both C_2H_6 and $C_4H_7^+$ are formed, the latter of which can either form a surface-bound alkyl (C_4H_7–Z) with a positive free energy of 25 kJ mol^{-1} or easily deprotonate to form C_4H_6 [62]. The transition state forms most easily in the 10-MR with C_4H_8 positioned in the channel intersection and $C_2H_5^+$ residing primarily in the straight channel and interacting with O16 (Fig. 1c). Previous computational studies have investigated hydride transfer reactions between surface-bound alkyls and hydrogen donors on 3 T zeolite cluster models (B3LYP) [87], phosphotungstic acid (PW-91) [88], and H-MOR (PW-91) [89]. These studies demonstrated that the hydride transfer transition state involves cleavage of the C–O bond and formation of a shared hydride intermediate state, in good agreement with the transition state shown in Fig. 1c. The most favorable transition state at O25, which is also the most favorable O-site to form C_2H_5–Z, has an intrinsic barrier 6 kJ mol^{-1} lower than that of O16.

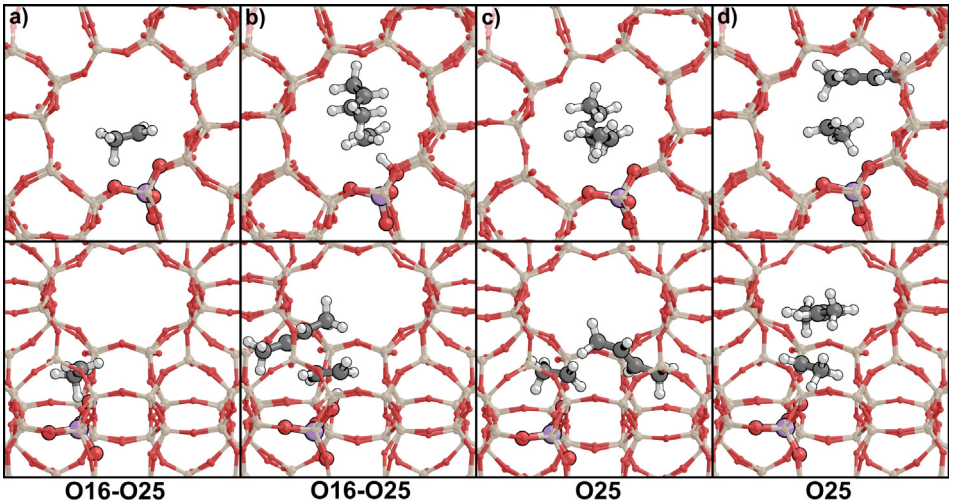

	O16-O25 C_2H_5–Z Formation	O16-O25 C_2H_5–Z Formation with C_4H_8	O25 C_2H_5–Z Hydride Transfer	O25 Concerted Hydride Transfer
ΔH	18 *(68)*	−18 *(63)*	−44 *(70)*	−38 *(43)*
ΔS	−161 *(−34)*	−332 *(−45)*	−303 *(21)*	−315 *(−28)*
ΔG	88 *(83)*	126 *(83)*	88 *(61)*	98 *(55)*

Fig. 1. Lowest energy transition state of a) C_2H_5–Z formation, b) C_2H_5–Z formation with spectating C_4H_8, c) C_2H_5–Z hydride transfer, and d) concerted hydride transfer viewed through the straight (top) and sinusoidal (bottom) channels in MFI. Effective enthalpy (ΔH, kJ mol^{-1}), entropy (ΔS, J mol^{-1} K^{-1}), and free energy (ΔG, kJ mol^{-1}) barriers are reported at 433 K and relative to a bare acid site (proton) and stoichiometric amounts of gas-phase C_2H_4 and C_4H_8. Intrinsic enthalpy, entropy, and free energy barriers are also given as *(ΔE_{act})* in italics. Dashed lines represent breaking and forming bonds.

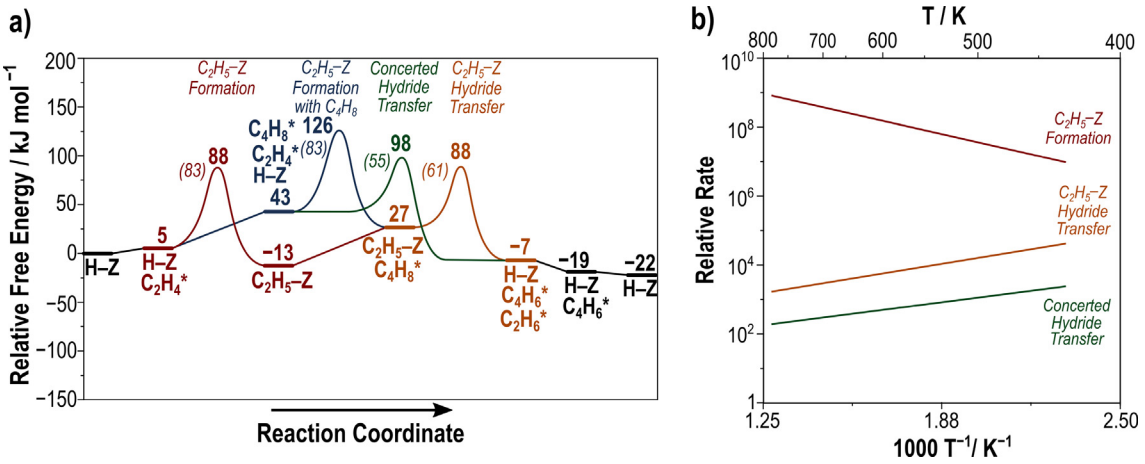

Fig. 2. a) Reaction coordinate diagram of the sequential and concerted mechanisms for alkene-mediated pathway in MFI. Free energies (kJ mol^{-1}, 433 K) relative to a bare acid site (proton) and intrinsic free energy barriers (in italics) are included. **b)** Rates of C_2H_5–Z formation (red), C_2H_5–Z hydride transfer (orange), and concerted hydride transfer (green) relative to the rate of C_2H_5–Z formation with co-adsorbed C_4H_8, the lowest rate according to maximum rate analysis, from 433 to 783 K at 0.004 bar C_2H_4 and 0.004 bar C_4H_8. Associated reactant, product, and transition state images associated are shown in Fig. 1 and Section S4. Rate equations are defined in Section S3. An enthalpy reaction coordinate diagram is included in the SI as Fig. S38. Maximum rate analysis is included in Section S17 of the SI. (For interpretation of the references to colour in this figure legend, the reader is referred to the web version of this article.)

Intrinsic barriers for this reaction at O14 are at least 51 kJ mol^{-1} higher than at O16 (Fig. S5) or at O25—this is likely because O16 and O25 have a similar chemical environment, both bridging the straight channel and the channel intersection, suggesting that such environment is favorable for these transition states. Here (and in the following sections), intrinsic and effective barriers are relative to the most stable surface-bound alkyl or bare proton state, respectively—regardless of O-site. Double bond isomerization is quasi-equilibrated during MTO [90] and likely occurs through the quasi-equilibrated formation of surface-bound alkyls; therefore, surface-bound alkyl interconversion is likely rapid between the accessible O-sites. As such, intrinsic barriers are calculated relative to the lowest energy alkyl (regardless of O-site) for each state. Furthermore, proton locations are also quasi-equilibrated during MTO, because proton carriers (methanol and water, for example) and alkyl-formation steps can shuttle protons between O-sites; therefore, effective energy barriers are calculated relative to the most stable H–Z state (at O14).

Single-step concerted hydride transfer occurs with a ΔG_{act} of 55 kJ mol^{-1} (Fig. 1d), slightly lower than that for the hydride transfer reaction which starts from a more stable surface-bound alkyl reactant. The transition state of the single-step concerted mechanism, in which C_2H_4 undergoes a simultaneous protonation from the surface and hydride transfer from C_4H_8, is most stable when positioned in the channel intersection and protonated from O25 (Fig. 1d). The converged structure shows that the proton transfer is nearly complete at the transition state, suggesting that the difficult step of this sequence is the hydride transfer. The partial negative charge of O16, which also interacts with the $C_2H_5^+$ intermediate, stabilizes the transition state by improving effective charge distribution. In the lowest energy transition state at O14, which has an energy 30 kJ mol^{-1} higher, $C_2H_5^+$ forms in the straight channel and interacts exclusively with O14, the oxygen from which it is protonated (Fig. S6). The transition state energies for the concerted and hydride transfer step of the sequential mechanism are within 10 kJ mol^{-1}, and the transition states have similar structures.

DFT-predicted effective free energy barriers ($\Delta G^{\neq}$) are calculated for the most favorable transition state of each reaction relative to a bare acid site (proton) (Fig. 2a). We interpret these effective barriers using maximum rate analysis to calculate maximum rates at conditions relevant to MTO (433–700 K, 0.004 bar C_2H_4 and C_4H_8), as explained in Section S17 in the SI. However, incomplete site balances necessary to simplify maximum rate analysis cause errors in the predictions of absolute rates. Instead, we can divide the maximum rate of each step by the maximum rate of the slowest overall step, C_2H_5–Z formation with co-adsorbed C_4H_8 (Fig. S44), to cancel out site balances (derived in Section S3) and compare relative maximum rates for elementary steps relevant to the alkene-mediated route (Fig. 2b). The first comparison is between the two steps in the sequential mechanism: C_2H_5–Z formation in an empty pore and C_2H_5–Z hydride transfer, and the sequential nature of these steps means that the step with the lowest rate will be rate-determining. The relative rate of C_2H_5–Z formation is at least 10^3-times higher than C_2H_5–Z hydride transfer (Fig. 2b), indicating that C_2H_5–Z hydride transfer is the rate-determining step of the sequential mechanism. Next, we compare the rate of sequential hydride transfer to the rate of concerted hydride transfer. Both hydride transfers have comparable transition state structures, and the C_2H_5–Z hydride transfer is predicted to be just 10-times faster than the concerted hydride transfer (Fig. 2b). We will assume that the alkene-mediated route in MFI is likely to occur via the sequential pathway (although errors associated with DFT mean the concerted pathway may also contribute) and is limited by C_2H_5–Z hydride transfer to compare the alkene-mediated pathway to the CH_2O-mediated pathway. The rate equation for the alkene-mediated route with rate and equilibrium constants defined by the sequential pathway is given by:

$$\frac{r}{[L]} = k_{HT,C_2H_5-Z} K_{C_2H_5-Z} K_{C_2H_4} K'_{C_4H_8} (C_2H_4)(C_4H_8) \frac{[*]}{[L]} \qquad (10)$$

where rate constants are defined in Scheme 1 and [*]/[L] represents the fraction of bare protons on the catalyst surface. Next, we consider the CHA framework (H-SSZ-13), which is also frequently studied as an MTO catalyst.

3.2. Alkene-mediated pathway in CHA

The MFI framework is susceptible to restructuring during DFT optimizations, which may produce artifacts in DFT calculated energies [75]; therefore, the same sequential (Eqs. (2) and (3)) and concerted mechanisms (Eq. (1)) for the alkene-mediated route were also studied in CHA to corroborate our findings in MFI. A detailed

description of the structures, analogous to the discussion in Section 3.1, can be found in the SI (Section S12). Intrinsic and effective free energy barriers in MFI and CHA are listed in Table S3 for comparison. C_2H_5–Z formation occurs in CHA with an intrinsic barrier (ΔG_{act}) of 86 kJ mol^{-1} (Fig. 3a), and the addition of spectating C_4H_8 leaves the intrinsic barrier effectively unchanged (84 kJ mol^{-1}, Fig. 3b). These intrinsic barriers are comparable to those observed in MFI (83 kJ mol^{-1}, Fig. 1), but more importantly they further suggest that spectating C_4H_8 does not facilitate C_2H_5–Z formation in CHA, similarly to MFI. The second step of the sequential mechanism, the hydride transfer between C_4H_8 and C_2H_5–Z, has a ΔG_{act} of 78 kJ mol^{-1} (Fig. 3c), and the concerted hydride transfer has a ΔG_{act} of 74 kJ mol^{-1} (Fig. 3d). Although the intrinsic barriers are higher for these two reactions in CHA than MFI (by 19 and 17 kJ mol^{-1}, respectively), both hydride transfers have similar transition state structures as those observed in MFI and have ΔG_{act} values within 10 kJ mol^{-1} of each other. Intrinsic free energy barriers in MFI and CHA are similar; however, effective free energy barriers ($\Delta G^{\neq}$) are generally 5–15 kJ mol^{-1} lower in CHA than MFI for reactions in the alkene-mediated route. We suspect that the lower effective barriers in CHA are the result of more exothermic alkene adsorptions in CHA given by the smaller rings (8-MR vs. 10-MR) which stabilize many of these intermediates and transition states. These differences in CHA and MFI do not alter our primary conclusions drawn from both frameworks: that intrinsic barriers for C_2H_5–Z formation are unaffected by spectating C_4H_8 and the concerted and sequential hydride transfers occur with similar transition state structures and intrinsic barriers.

Effective free energy barriers relative to a bare acid site (Fig. 4) were again used to perform maximum rate analysis and compare relative rates for each step of the alkene-mediated pathway in CHA. Rates were calculated and analyzed following the same procedures used in MFI, which are described in detail for CHA in Section S17 of the SI. Comparing the relative rates of each step, the results in CHA further corroborate those observed for MFI: the sequential mechanism is controlled by the rate of C_2H_5–Z hydride transfer, and the maximum rates of sequential and concerted hydride transfers are essentially identical (Fig. S41). The rate of C_2H_5–Z hydride transfer is 10-times faster than the rate of concerted hydride transfer (Fig. S41), and we will again assume the sequential mechanism dominates for the purposes of comparison to the CH_2O-mediated pathway. The rate equation of the alkene-mediated pathway in CHA is the same as that derived for MFI in Eq. (10). In both frameworks, the alkene-mediated route is governed by the rate of hydride transfer between butene and a surface-bound alkyl.

3.3. CH_2O-mediated pathway in MFI

Diene formation can also occur via a CH_2O-mediated route (Scheme 2). Analogously to the alkene-mediated pathway (Section 3.2), the CH_2O-mediated pathway was investigated by a sequential mechanism (Eqs. (4)–(6)) where CH_3OH adsorbs and reacts with a proton to form a surface-bound methyl, CH_3–Z, which subsequently reacts with a second CH_3OH to form CH_2OH–Z (Scheme 2). Alternatively, a concerted mechanism can occur where two CH_3OH directly react with each other to form CH_2O then CH_2-OH–Z (Scheme 2). Once CH_2OH–Z is formed, it can react with propene (C_3H_6) to form butenol (C_4H_7OH). Finally, butenol can dehydrate to form butadiene (Scheme 2). Critical states and rate constants are defined in Scheme 2 and used in maximum rate analysis at the end of this section and in Section S3 of the Supplemental Information. This Section and Section 3.4 focus on CH_2O-mediated routes with the smallest possible reactants; however, it is possible for these reactions to occur with a variety of surface-bound alkyls, particularly the sequential route, which are further discussed in Section 3.5.

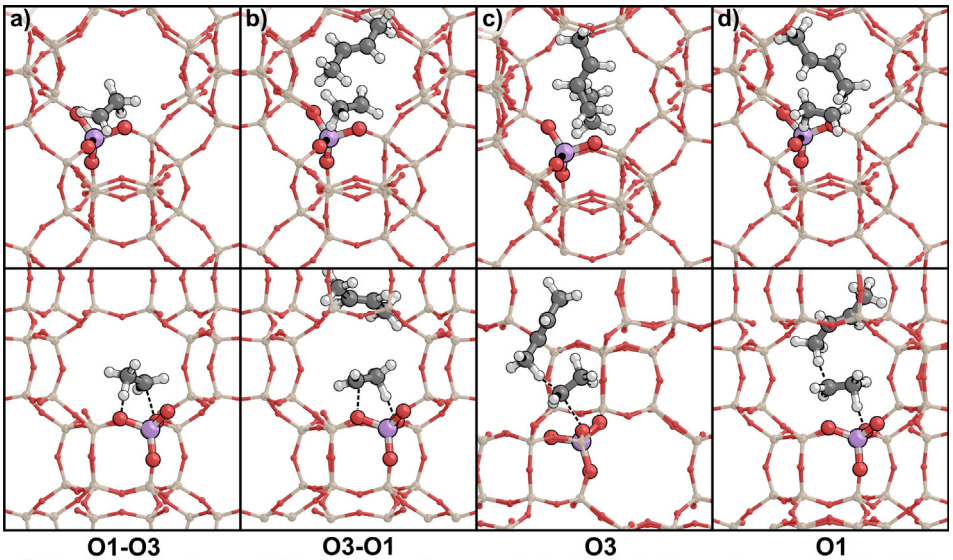

	O1-O3 C_2H_5–Z Formation	O3-O1 C_2H_5–Z Formation with C_4H_8	O3 C_2H_5–Z Hydride Transfer	O1 Concerted Hydride Transfer
ΔH	9 *(72)*	−38 *(67)*	−65 *(74)*	−50 *(55)*
ΔS	−173 *(−33)*	−312 *(−38)*	−325 *(−9)*	−317 *(−43)*
ΔG	83 *(86)*	97 *(84)*	75 *(78)*	87 *(74)*

Fig. 3. Lowest energy transition state of a) C_2H_5–Z formation, b) C_2H_5–Z formation with spectating C_4H_8, c) C_2H_5–Z hydride transfer, and d) concerted hydride transfer in CHA. Effective enthalpy (ΔH, kJ mol^{-1}), entropy (ΔS, J mol^{-1} K^{-1}), and free energy (ΔG, kJ mol^{-1}) barriers are reported at 433 K and relative to a bare acid site (proton) and stoichiometric amounts of gas-phase C_2H_4 and C_4H_8. Intrinsic enthalpy, entropy, and free energy barriers are also given as *(ΔE_{act})* in italics. Dashed lines represent breaking and forming bonds.

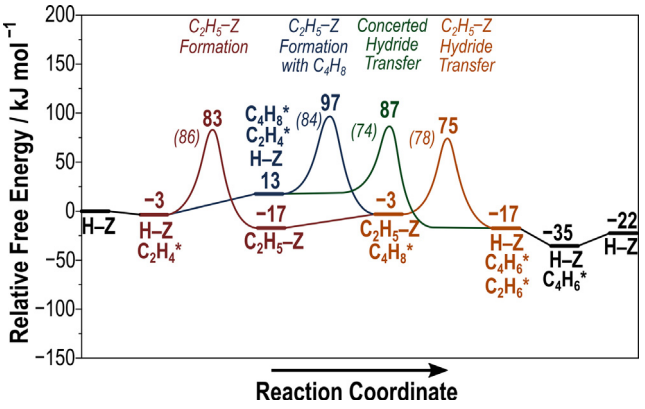

Fig. 4. Reaction coordinate diagram (RCD) of the sequential and concerted mechanism for the alkene-mediated pathway in CHA. Free energies (kJ mol^{-1}, 433 K) are relative to a bare acid site (proton) and stoichiometric amounts of gas-phase C_2H_4, and C_4H_8. Intrinsic free energy barriers are included in italics. Reactant, product, and transition state images associated with this RCD are partly shown in Fig. 2 and Section S10 of the Supplemental Information. Rate equations are defined in Section S3. An enthalpy reaction coordinate diagram is included in the SI as Fig. S39. Maximum rate analysis and relative rates are included in Section S17 of the SI.

The first step of the sequential mechanism is the dehydration of CH_3OH to form a surface-bound methyl species (CH_3–Z) (Eq. (4)), and this reaction has been extensively studied in prior work [77,79,91–93]. This transition state preferentially forms a C–O bond with O16 in the 10-MR adjacent to the channel intersection, where it is stabilized by dispersive forces and hydrogen bonding between H_2O and framework oxygens (Fig. 5a), occurring with a ΔG_{act} of 129 kJ mol^{-1}. This intrinsic barrier is comparable to those reported for CH_3–Z formation in MFI (126 kJ mol^{-1}) by previous computational studies [77,79]. In this work, CH_3–Z formation is investigated with CH_3OH as the methylation agent because it is unlikely this step controls the rate. Other species, particularly

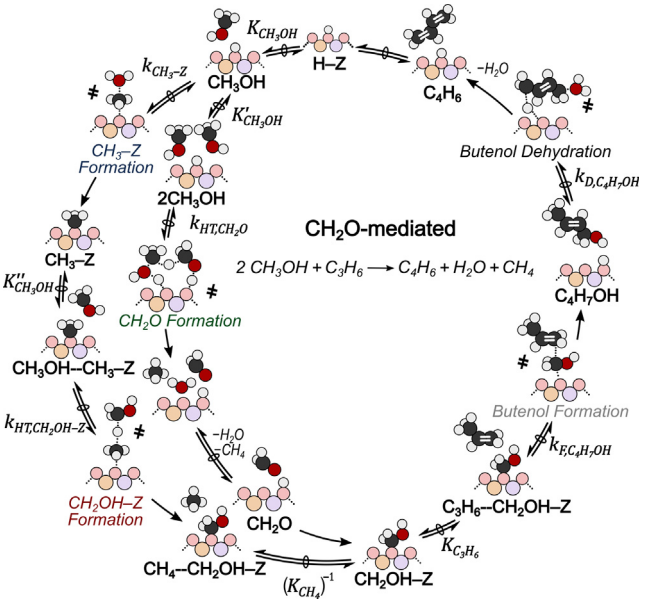

Scheme 2. CH_2O-mediated diene formation showing both sequential and concerted CH_2OH–Z mechanisms. Critical transition states CH_3–Z formation (blue), CH_2OH–Z formation (hydride transfer, red), CH_2O formation (hydride transfer, green), butenol formation (gray), and butenol dehydration (black) are labeled. The CH_2O protonation transition state is omitted to simplify the scheme. Rate constants used in Eq. (11) and Section S3 of the Supplemental Information are shown here.

CH_3OCH_3, are also capable of methylating the zeolite surface, and may do so at higher rates than CH_3OH [53,79,94].

The second step of the sequential mechanism is the quasi-equilibrated adsorption of a second CH_3OH, followed by a hydride transfer reaction between CH_3OH and CH_3–Z to form hydroxymethyl (CH_2OH–Z) and CH_4 (Eq. (5)). The transition state involves the cleavage of the C–O framework bond and concurrent hydride transfer from CH_3OH to CH_3^+ (Fig. 5b). The most stable transition state occurs with a ΔG_{act} of 102 kJ mol^{-1} and forms at O25, where it is solvated by the 10-MR and stabilized by hydrogen bonding between CH_3OH and a framework oxygen (186 pm, Fig. 5b). The most stable transition state at O16 forms in the same 10-MR at the channel intersection, but the hydrogen bond to the framework is slightly longer (191 pm, Fig. S10), contributing to an energy 11 kJ mol^{-1} higher than O25. The optimal transition state at O14 has a shorter hydrogen bond (183 pm, Fig. S10), but framework strain at O14 causes this transition state to be 38 kJ mol^{-1} higher than the most stable transition state (Fig. S10).

Formaldehyde formation can also proceed by a concerted mechanism, in which two CH_3OH molecules directly react to form CH_2O, H_2O, and CH_4 (Eq. (7))—without forming CH_3–Z or the associated H_2O desorption. The transition state preferentially forms at O25 in the channel intersection (Fig. 5c) and involves a CH_3^+ species accepting a hydride from CH_3OH and the concurrent cleavage of a C–O bond to form H_2O. In the most favorable configuration, H_2O forms a hydrogen bond with O25 (166 pm, Fig. 5c) and CH_3OH hydrogen bonds with a framework oxygen (244 pm, Fig. 5c), indicating a preference for structures which form strong hydrogen bonds to the zeolite framework. This reaction occurs with a higher intrinsic barrier (ΔG_{act} of 162 kJ mol^{-1}) than hydride transfer in the sequential reaction (102 kJ mol^{-1}), in part because it is starting from a more thermodynamically favorable state.

The sequential and concerted mechanisms form slightly different products, with the former forming CH_2OH–Z (hydroxymethyl) and the latter forming CH_2O. Surface-bound CH_2OH–Z species can undergo a reaction to form CH_2O and a protonated surface (H–Z). The transition state requires simultaneous interaction with two oxygens: one oxygen where the C–O framework bond is broken and a second oxygen that is protonated by the CH_2OH^+ species. The most favorable transition state resides in the straight channel, where the C–O bond is cleaved at O16 and O14 is protonated (Fig. 5d). The reaction occurs with a ΔG_{act} of 69 kJ mol^{-1} (Fig. 5d), suggesting that the interconversion between CH_2OH–Z and CH_2O is likely quasi-equilibrated. The energy of CH_2OH–Z is 25 kJ mol^{-1} higher than the energy of CH_2O (Fig. 6), therefore formaldehyde likely exists as an adsorbed species in the pore instead of CH_2OH–Z.

CH_2OH–Z can subsequently react with an alkene (Eqs. (8) and (9)), such as propene, to form an alkenol. The reaction with propene forms butenol (Fig. 5e), which dehydrates to form butadiene (Fig. 5f). Butenol forms most favorably at O16, where it is stabilized by dispersive interactions with the 10-MR and hydrogen bonding to framework oxygens (200 pm, Fig. 5e). Dehydration also occurs preferentially at O16 and is solvated by the 10-MR; however, $C_4H_7^+$ is positioned in the straight channel instead of the intersection (Fig. 5f). These reactions occur with a ΔG_{act} of 31 kJ mol^{-1} and 79 kJ mol^{-1}, respectively (Fig. 6).

Following the same procedure used for the alkene-mediated pathway, maximum rate analysis was performed for the CH_2O-mediated route (Section S17). The slowest step in this pathway, according to maximum rate analysis, is concerted CH_2O formation, and all relative rates are divided by the maximum rate of this step (Fig. 7). First, we can compare the relative rates of the first two steps of the sequential mechanism, CH_3–Z formation and CH_2-OH–Z formation. The $\Delta G^{\ddagger}$ of CH_2OH–Z formation is 17 kJ mol^{-1} higher (Fig. 6) and the rate is 10-times lower than CH_3–Z formation

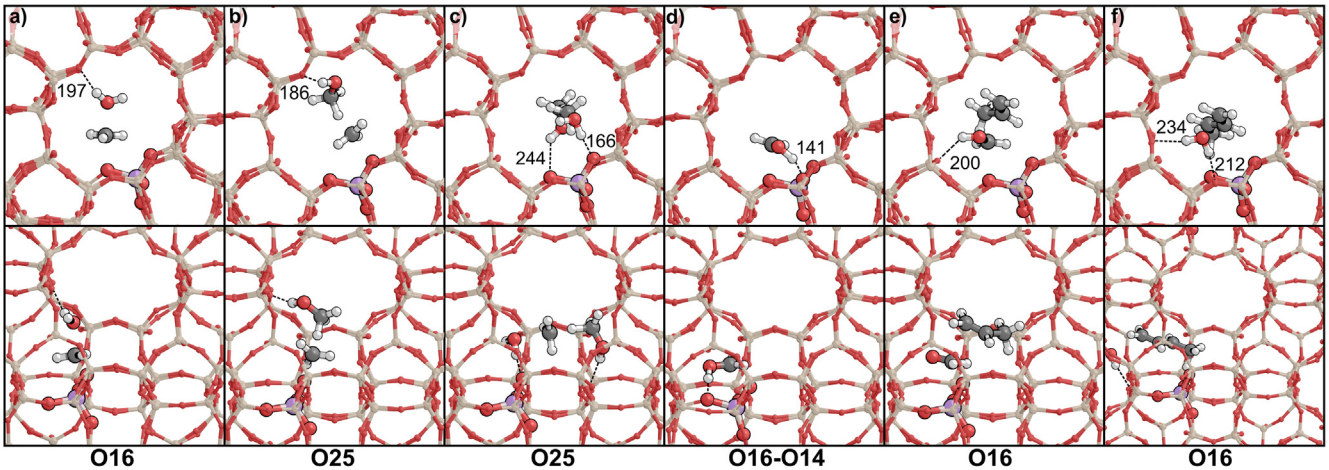

	O16 CH_3–Z Formation	O25 CH_2OH–Z Formation	O25 Concerted CH_2O Formation	O16-O14 CH_2O Protonation	O16 Butenol Formation	O16 Dehydration
ΔH	37 *(119)*	50 *(83)*	15 *(156)*	−26 *(51)*	−87 *(34)*	−130 *(90)*
ΔS	−169 *(−22)*	−177 *(−44)*	−300 *(−15)*	−58 *(−42)*	−188 *(6)*	−181 *(26)*
ΔG	110 *(129)*	127 *(102)*	145 *(162)*	−1 *(69)*	−5 *(32)*	−51 *(79)*

Fig. 5. Lowest energy transition state of a) CH_3–Z formation, b) CH_2OH–Z formation, c) concerted CH_2O formation, d) CH_2O protonation, e) butenol formation, and f) butenol dehydration viewed through the straight (top) and sinusoidal (bottom) channels in MFI. Effective enthalpy (ΔH, kJ mol^{-1}), entropy (ΔS, J mol^{-1} K^{-1}), and free energy (ΔG, kJ mol^{-1}) barriers are reported at 433 K and relative to a bare acid site (proton) and stoichiometric amounts of gas-phase CH_3OH and C_3H_6. Intrinsic enthalpy, entropy, and free energy barriers are also given as *(ΔE_{act})* in italics. Dashed lines on top images represent hydrogen bonding, and dashed lines on bottom images represent breaking and forming bonds.

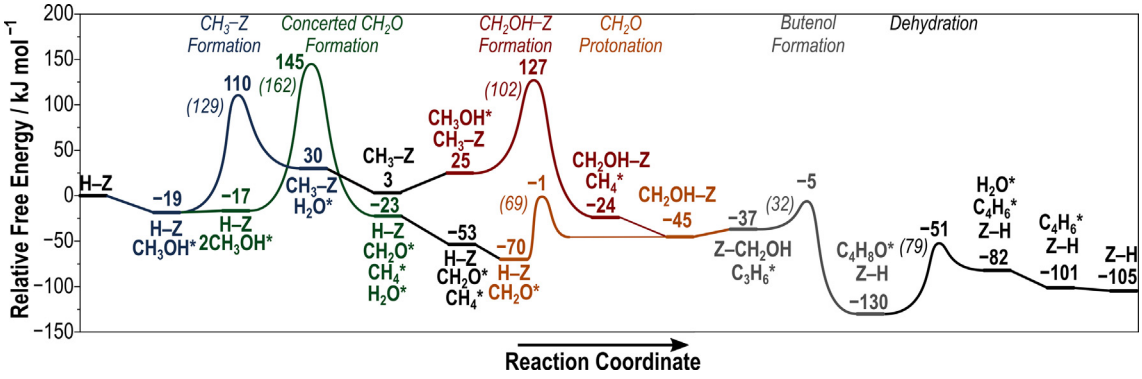

Fig. 6. Reaction coordinate diagram of the sequential and concerted pathways for the CH_2O-mediated route in MFI. Free energies (kJ mol^{-1}, 433 K) are relative to a bare acid site (proton) and stoichiometric amounts of gas-phase CH_3OH and C_3H_6. Intrinsic free energy barriers are included in italics. Associated reactant, product, and transition state images are shown in Fig. 5 and Section S10. An enthalpy reaction coordinate diagram is included in the SI as Fig. S40.

(Fig. 7); because these two steps are in series, we can conclude that CH_2OH–Z formation is rate determining for sequential formaldehyde formation. The rate of CH_2OH–Z formation is then compared to the relative rate of the remaining steps, all of which occur in series, to establish the rate determining step of the entire CH_2O-mediated pathway. CH_2O protonation, butenol formation, and dehydration occur with a $\Delta G^{\ddagger}$ 128 kJ mol^{-1}, 126 kJ mol^{-1}, and 172 kJ mol^{-1} (Fig. 6) lower than CH_2OH–Z formation and are entropically benefited by H_2O and CH_4 desorption. As a result, these steps have relative rates >10^{10}-fold faster than CH_2OH–Z formation (Fig. 7) and are kinetically irrelevant. This indicates that CH_2O is highly reactive upon formation and can readily form dienes in the presence of small amounts of propene, likely contributing to its miniscule concentrations during MTO processes. CH_2OH–Z formation, the rate determining step of the CH_2O-mediated pathway, involves a hydride transfer between CH_3OH and a surface-bound alkyl (CH_3–Z) and is analogous to the rate-determining transition state in the alkene-mediated route where C_4H_8 transfers a hydride to a surface-bound alkyl (C_2H_5–Z). The rate equation governing the CH_2O-mediated pathway in MFI is defined as:

$$\frac{r}{[L]} = k_{HT,CH_2OH-Z} K_{CH_3OH} K''_{CH_3OH} (CH_3OH)^2 (H_2O)^{-1} \frac{[*]}{[L]} \quad (11)$$

where K_{CH3OH} represents adsorption of CH_3OH, K_{alkyl} represents formation of CH_3–Z, K''_{CH3OH} represents adsorption of CH_3OH near CH_3–Z, and $k_{HT,CH2OH-Z}$ represents reaction of CH_3–Z with CH_3OH to form CH_2OH–Z as defined in Scheme 2. This reaction is analogous to Eq. (10) and modified versions of these two rate equations are used to compare the CH_2O-mediated and alkene-mediated pathways in Section 3.5.

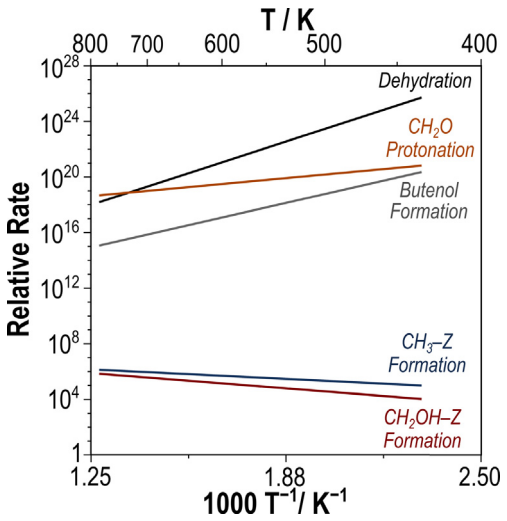

Fig. 7. Rates of CH_3–Z formation (blue), CH_2OH–Z formation (blue), CH_2O protonation (orange), butenol formation (gray), and dehydration (black) relative to the rate of concerted CH_2O formation, the lowest rate according to maximum rate analysis, from 433 to 783 K at 0.1 bar CH_3OH, 0.01 bar H_2O, 0.01 bar CH_4, and 0.1 bar C_3H_6. Maximum rate analysis is included in Section S17. (For interpretation of the references to colour in this figure legend, the reader is referred to the web version of this article.)

3.4. CH_2O-mediated pathway in CHA

The CH_2O-mediated pathway was also investigated in CHA, with the same sequential mechanism (Eqs. (5) and (6)) and concerted mechanism (Eq. (7)) as in MFI (Section 3.3). An in-depth description of the transition state structures can be found in Section S13, and intrinsic and effective free energy barriers in MFI and CHA are included in Table S3 for comparison. We find that the dehydration of CH_3OH to form CH_3–Z, the first step of the sequential mechanism, occurs with a ΔG_{act} of 130 kJ mol^{-1} (Fig. 8a), almost identical to the ΔG_{act} of the same step in MFI (129 kJ mol^{-1}, Fig. 5a). This intrinsic barrier has been previously calculated using the PBE-D3 function and reported as 171 kJ mol^{-1} at 673 K [95]; our predicted ΔG_{act} at 673 K is substantially lower at 132 kJ mol^{-1}, and we believe this difference originates from our systematic reorientation approach. The intrinsic barrier for CH_2OH–Z formation in CHA (101 kJ mol^{-1}, Fig. 8b) is again essentially the same as in MFI (102 kJ mol^{-1}, Fig. 5b). Although concerted CH_2O formation has a higher intrinsic barrier than sequential CH_2OH–Z formation in both frameworks, the ΔG_{act} of the reaction in CHA (143 kJ mol^{-1}, Fig. 8c) is 18 kJ mol^{-1} lower than in MFI. We attribute this decrease in ΔG_{act} to the increased number of hydrogen bonds and the stronger average hydrogen bonding in the transition state in CHA (188 pm (Fig. 8c) versus 205 pm (Fig. 5c)). In all reactions, the effective barriers are lower than intrinsic, which arise because of a combination of strong hydrogen bonds between –OH groups and the Bronsted acid site and entropic benefits of CH_4 and H_2O desorption, as is the case in MFI (Fig. 8d–f).

Following the same trend observed for the alkene-mediated route, effective free energy barriers ($\Delta G^{\neq}$) for the CH_2O-mediated pathway are 10–32 kJ mol^{-1} lower in CHA than MFI (Fig. 9), excluding butenol dehydration, which is 17 kJ mol^{-1} higher (Table S3). Prior investigations have reported that charged transition states are more effectively solvated by void environments that approach the size of the transition state complex [96–98]. Just as we discussed for the alkene-mediated route, it is our view that the lower effective barriers result from enhanced stabilization of these relatively small transition states in the 8-MRs of CHA compared to the larger 10-MRs in MFI. We also consider lower effective barriers for diene formation to be consistent with experimental observations that the aromatic cycle of MTO is favored in small pore zeolites such as CHA, as dienes are aromatic precursors [59]. Because the reactions investigated in this work comprise only a subset of the reactions that occur during MTO, we cannot confidently make overarching conclusions regarding catalyst selectivity. Despite differences in effective barriers, our data in CHA corroborate the results obtained in MFI for the CH_2O-mediated pathway and suggest that the mechanism of diene formation will be similar for the two zeolite frameworks.

Maximum rate analysis and relative rates, explained in depth in Section S17 of the SI, were used to find the dominant mechanism of the CH_2O-mediated pathway in CHA. Analysis of relative rates in CHA supports the same conclusions made in MFI, just as rates in CHA followed the same trends in MFI for the alkene-mediated pathway. In both frameworks, we find that formaldehyde is formed via the sequential pathway and CH_2OH–Z formation is the rate determining step of the entire CH_2O-mediated route (Fig. S46). The rate of butadiene formation via CH_2O-mediated pathways in CHA is governed by the same rate equation (Eq. (11)) as derived in Section 3.3.

3.5. Effect of alkyl size on Alkene-mediated and CH_2O-mediated pathways

Alkene-mediated and CH_2O-mediated routes have been discussed with C_2H_5–Z and CH_3–Z, respectively, as hydride acceptors. However, larger surface-bound alkyls can be formed from the protonation of MTO product alkenes or through dealkylation (of e.g., CH_3OCH_3 or CH_3OH) or cracking reactions during MTO. A given alkyl can react with a $C_{\geq 4}$ alkene to form an alkane and diene or with CH_3OH to form CH_2O and ultimately dienes (Scheme 3). Here, we examine both hydride transfer reactions with five representative alkyls species: methyl, ethyl, propyl, *sec*-butyl, and *tert*-butyl.

The formation of the hydride transfer transition state, relative to the adsorbed alkyl (CR_3–Z), is given by:

$$\Delta G_a^{\neq} = G[TS^{\neq}] - G[CR_3\text{–}Z] - G[\text{donor(g)}] \quad (12)$$

where G[TS≠] is the energy of the hydride transfer transition state (CH_3OH--CR_3–Z or C_4H_8--CR_3–Z, Scheme 3), G[CR_3–Z] is the energy of the surface-bound alkyl, and G[donor(g)] is the energy of the gas-phase hydride donor (CH_3OH or C_4H_8). The lowest CH_3OH hydride transfer barrier ($\Delta G_a^{\neq}$) is with *tert*-butyl as the acceptor, and this reaction has a $\Delta G_a^{\neq}$ of 55 kJ mol^{-1} in MFI and 104 kJ mol^{-1} in CHA (Fig. 10). CH_2O-mediated $\Delta G_a^{\neq}$ barriers inversely trend with carbocation stability, where $\Delta G_a^{\neq}$ barriers follow the sequence: primary (1°) > secondary (2°) > tertiary (3°). This same trend has been observed in diene hydrogenation effective barriers [62] as well as alkene alkylation [31,99]. Notably, *tert*-butyl transition states in MFI are 45 kJ mol^{-1} more stable than all other transition states, while the *tert*-butyl transition state in CHA is only favored by 4 kJ mol^{-1} when reacting with CH_3OH (Fig. 10). The exact reason for this is unclear, but we hypothesize it is related to the proximity of the transition state to the surrounding framework. The channel intersection in MFI is surrounded by 10-MRs large enough to partially accommodate and stabilize a transition state complex, as evinced by transition states for the hydride transfer between CH_3OH and the other alkyls in which the alkyl carbocation resides at the edge of the channel intersection (Fig. S12). The *tert*-butyl transition state in MFI is in a similar but inverted position with the larger *tert*-butyl alkyl in the channel intersection and the smaller CH_2O species stabilized by hydrogen bonding (169 pm, Fig. S12) at the edge of the 10-MR. Although the CHA cage has larger diameter (~7.3 Å in CHA versus ~6.4 Å in MFI) [76], bulky adsorbates residing within CHA are constricted by the smaller 8-MRs that surround the

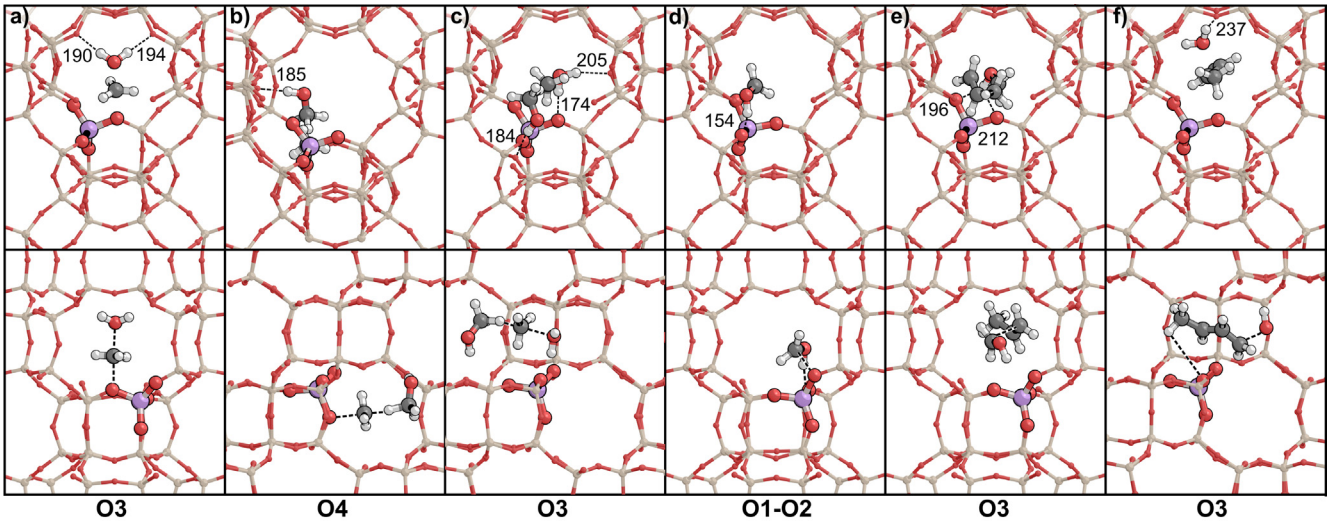

	O3 CH_3–Z Formation	O4 CH_2OH–Z Formation	O3 Concerted CH_2O Formation	O1-O2 CH_2O Protonation	O3 Butenol Formation	O3 Dehydration
ΔH	10 *(126)*	35 *(85)*	−29 *(121)*	−48 *(41)*	−118 *(11)*	−115 *(130)*
ΔS	−176 *(−9)*	−189 *(−35)*	−329 *(−49)*	−74 *(−51)*	−202 *(−24)*	−201 *(18)*
ΔG	86 *(130)*	117 *(101)*	114 *(143)*	−15 *(64)*	−31 *(21)*	−28 *(122)*

Fig. 8. Lowest energy transition state of a) CH_3–Z formation, b) CH_2OH–Z formation, c) concerted CH_2O formation, d) CH_2O protonation, e) butenol formation, and f) butenol dehydration in CHA. Effective enthalpy (ΔH, kJ mol^{-1}), entropy (ΔS, J mol^{-1} K^{-1}), and free energy (ΔG, kJ mol^{-1}) barriers are reported at 433 K and relative to a bare acid site (proton) and stoichiometric amounts of gas-phase CH_3OH, H_2O, CH_4, and C_3H_6. Intrinsic enthalpy, entropy, and free energy barriers are also given as *(ΔE_{act})* in italics.

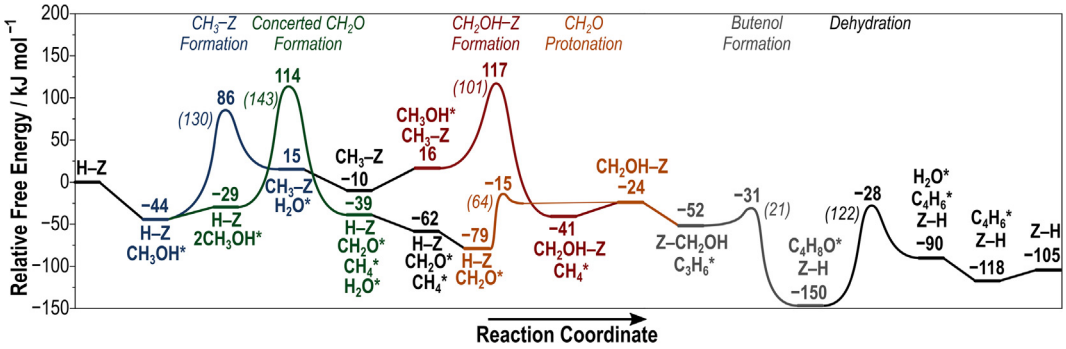

Fig. 9. Reaction coordinate diagram of the sequential and concerted pathways for the CH_2O-mediated route in CHA. Free energies (kJ mol^{-1}, 433 K) relative to a bare acid site (proton) and intrinsic free energy barriers (in italics) are included. Associated reactant, product, and transition state images are shown in Fig. 8 and Section S10. An enthalpy reaction coordinate diagram is included in the SI as Fig. S41. Maximum rate analysis and relative rates are included in Section S17.

CHA cage. The *tert*-butyl transition state in CHA is positioned closer to the framework than in MFI (Fig. S42, S43), incurring greater steric penalties that offset the enhanced carbocation stability and stronger hydrogen bonding (160 pm, Fig. S13). The differences in MFI and CHA are worth investigating; however, within the uncertainties of our DFT methods we feel it is best to focus on our overall conclusion—that hydride transfer barriers are lower for larger alkyls—which is the same for both frameworks.

Hydride transfer barriers between C_4H_8 and the 5 alkyl acceptors follow a similar trend to those for CH_3OH-alkyl reactions in that reactions via primary carbocations occur with higher $\Delta G_a^{\neq}$ barriers than those via secondary carbocations (Fig. 10). Tertiary carbocation structures, however, have hydride transfer barriers significantly higher than all other species ($\Delta G_a^{\neq}$ 156 kJ mol^{-1} in MFI and 192 kJ mol^{-1} in CHA), suggesting that the favorable effects conferred by enhanced carbocation stability are mitigated by unfavorable steric constraints for the hydride transfer between C_4H_8 and *tert*-butyl (a C_8 complex). This is especially notable in CHA, where *tert*-butyl transition states occur with $\Delta G_a^{\neq}$ barriers >40 kJ mol^{-1} higher than all other transition states. Analogous to the hydride transfer with CH_3OH, the transition states for the hydride transfer between C_4H_8 and alkyls in MFI are almost entirely positioned in the channel intersection to maximize non-covalent framework interactions. The exception is the *tert*-butyl transition state, as the bulky geometry of *tert*-butyl requires C_4H_8 to remain in the straight channel, where interactions are less optimal (Fig. S14). All transition states with C_4H_8 in CHA are stabilized by their proximity to an 8-MR to enhance non-covalent interactions (Fig. S15). Again, the exception is the *tert*-butyl transition state, in which C_4H_8 is located within an 8-MR because it is too large to fit favorably inside the cage with *tert*-butyl, resulting in a carbocation located further away from an 8-MR (Fig. S15). Analysis of $\Delta G_a^{\neq}$ barriers suggest that CH_3OH primarily reacts with *tert*-butyl surface-bound alkyls in both CHA and MFI, while C_4H_8 reacts with either propyl or *sec*-butyl alkyls. Prior work examining olefin:paraffin ratios on H-ZSM-5 (MFI framework) and H-SSZ-13 (CHA framework) demonstrated that H-ZSM-5 forms C_4–C_7 paraffins (6.4%

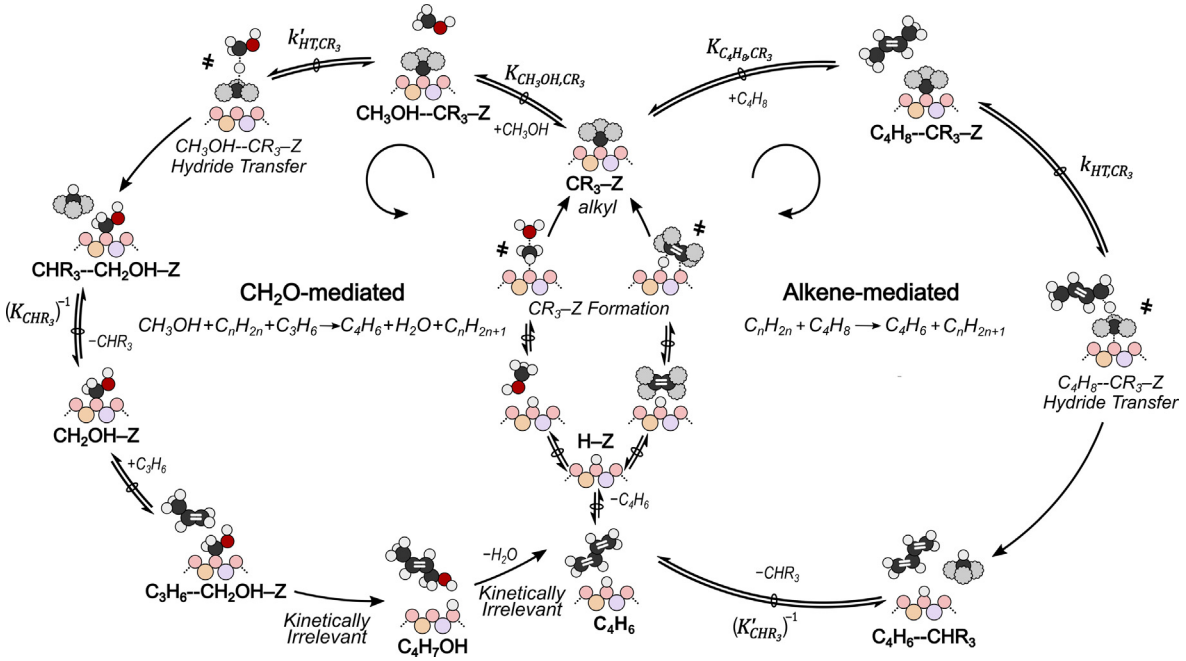

Scheme 3. Abbreviated mechanism of alkene-mediated and CH_2O-mediated diene formation routes demonstrating that surface-bound alkyls can participate in two competing hydride transfer mechanism. Steps shown with gray substituents, R, represent H, CH_3, or CH_2CH_3. Rate constants (k and K) used in Equations (13) and (15) are defined here. Surface-bound alkyls can be formed from either CH_3OH (to form CH_3–Z) or an alkene, such as C_2H_4 (which forms C_2H_5–Z). Alkyl species are represented as CR_3–Z and in the case of the alkene formation route, at least one R group will be $-CH_3$ or $-C_2H_5$. The hydride transfer transition state for each pathway (CH_3OH–CR_3–Z and C_4H_8–CR_3–Z) is the transition state used to calculate $\Delta G_a^{\neq}$ (Eq. (12)) relative to the CR_3–Z state and corresponding gas-phase species.

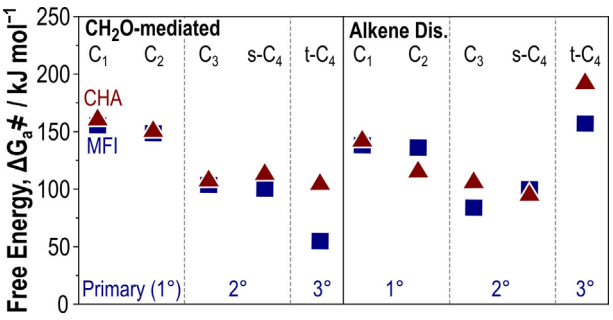

Fig. 10. Free energy ($\Delta G_a^{\neq}$) barriers (kJ mol^{-1}) for C_1 (methyl), C_2 (ethyl), C_3 (propyl), s-C_4 (*sec*-butyl), and t-C_4 (*tert*-butyl) reaction via CH_2O-mediated (left) and alkene-mediated routes (right) in MFI (blue, squares) and CHA (red, triangles). Reactions mediated by primary (1°), secondary (2°), and tertiary (3°) carbocations are grouped. Transition state structures associated with these states are shown in Section S8. (For interpretation of the references to colour in this figure legend, the reader is referred to the web version of this article.)

selectivity) with higher selectivity than C_2–C_3 paraffins (<1% selectivity) while H-SSZ-13 selectively forms C_2–C_3 paraffins (5.1% selectivity) over C_4–C_7 paraffins(<1% selectivity) [59]. The results presented here suggest that a possible explanation for differences in observed paraffin selectivities is that large, tertiary surface-bound alkyls act as hydride acceptors in MFI—resulting in the formation of larger C_4–C_7 alkanes observed experimentally. Conversely, these larger species can start to experience repulsive interactions in CHA, favoring hydride transfer between smaller, secondary surface-bound alkyls to form C_2–C_3 alkanes.

We can use these $\Delta G_a^{\neq}$ values to examine which surface-bound alkyls will dominate the two hydride transfer pathways at varying alkyl (CR_3–Z) concentrations by examining the hydride transfer rate (r_{HT}) ratio for a given alkyl to methyl (for either hydride donor):

$$\frac{r_{HT,CR_3\text{-}Z}}{r_{HT,CH_3\text{-}Z}} = \frac{k_{HT,CR_3} K_{donor,CR_3} [CR_3\text{-}Z]}{k_{HT,CH_3} K_{donor,CH_3} [CH_3\text{-}Z]} = e^{\frac{-(\Delta G_{CR_3}^{\neq} - \Delta G_{CH_3}^{\neq})}{RT}} \frac{[CR_3\text{-}Z]}{[CH_3\text{-}Z]} \quad (13)$$

where k_{HT,CR_3} is the rate constant for hydride transfer between the donor (CH_3OH or C_4H_8) and CR_3 alkyl, K_{donor,CR_3} is the co-adsorption equilibrium constant for the donor molecule near the CR_3 alkyl, and [CR_3–Z] is the concentration of the surface bound alkyl (with corresponding terms for CH_3). This rate ratio (Eq. (13)) can indicate which surface alkyls are likely to undergo hydride transfers to CH_2O or C_4H_6 during MTO, based on the ratio of surface alkyl concentrations present during the reaction, which depends on the conversion and selectivity of the catalyst. The rate ratio for CH_2O formation via *tert*-butyl to methyl exceeds 1 (favoring *tert*-butyl) at an alkyl ratio of 10^{-10} in MFI and 10^{-6} in CHA (Fig. 11a). We suspect the higher *tert*-butyl concentration required in CHA can be attributed to the previously discussed steric penalties incurred in the *tert*-butyl transition state, but the ratio of *tert*-butyl in both frameworks indicates that CH_2O is predominantly formed from CH_3OH reactions with $C_{\geq 2}$ alkyls instead of surface methyls. Previous work has shown that CH_2O and CH_4 are present in the effluent at reaction start-up in MFI [54], suggesting that CH_2O is formed via the reaction of CH_3–Z with CH_3OH before the formation of the hydrocarbon pool. Our findings do not contradict this experimental evidence but subvert the assumption made by prior studies that CH_3–Z remains the primary alkyl involved in hydrogen transfer with CH_3OH [32,53–54,100] for the duration of MTO. This preference for CH_2O formation via alkyls larger than methyl is also observed for *sec*-butyl, propyl, and ethyl, as their rate ratios (to methyl) exceed 1 at alkyl ratios as low as ~10^{-6} for species that react via secondary carbocations (*sec*-butyl and propyl) and ~10^{-2} for ethyl (Fig. 11a) which proceeds via a primary carbocation that is still more stable than the methyl carbocation. Our data suggest that once the hydrocarbon pool is present, CH_2O is formed by the reaction of CH_3OH with substituted $C_{\geq 2}$ alkyls formed from

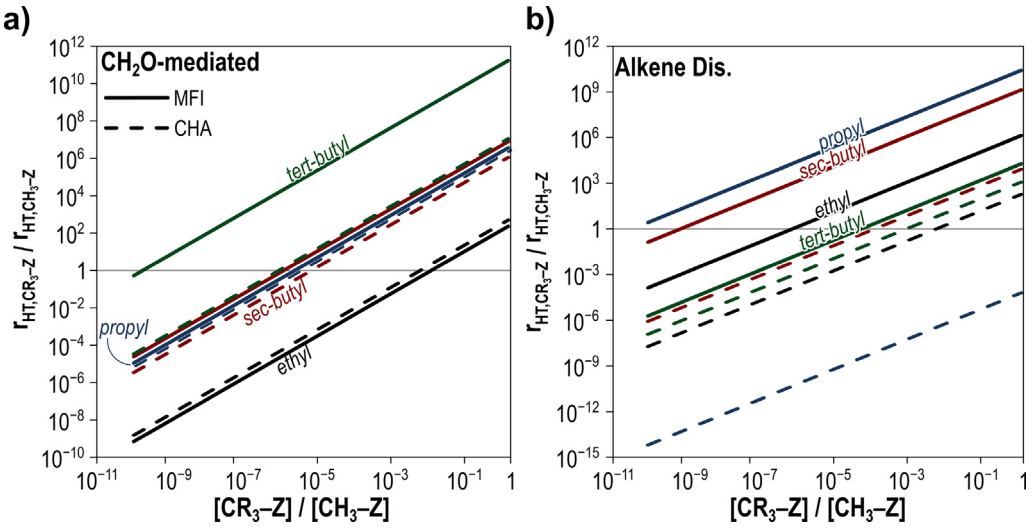

Fig. 11. **a)** Ratio of hydrogen transfer rates for *tert*-butyl (green), *sec*-butyl (red), propyl (blue), and ethyl (black) with CH_3OH to the rate of hydride transfer with methyl and CH_3OH in MFI and CHA (dashed) at 623 K. **b)** Ratio of hydrogen transfer rates for *tert*-butyl (blue), *sec*-butyl (red), propyl (green), and ethyl (black) with C_4H_8 to the rate of hydride transfer with methyl and C_4H_8 in MFI and CHA (dashed) at 623 K. A horizontal gray line at 1 is used to separate methyl-preferred reactions (below 1) and C_{2+}-preferred pathways (above 1). (For interpretation of the references to colour in this figure legend, the reader is referred to the web version of this article.)

product alkenes instead of with the CH_3–Z MASI, formed from CH_3OH or CH_3OCH_3 reactants. The implications of this finding are crucial for understanding catalyst deactivation during MTO, because the involvement of products in the formation of CH_2O means that reactor conversion (and potentially time-on-stream if larger tertiary alkenes become trapped) will have a significant impact on CH_2O formation rates. More broadly, our results reveal that surface intermediates of relatively low concentration may be critical when proposing mechanisms for process such as MTO in which potentially reactive products are present.

Substituted alkyls also react with C_4H_8 with lower $\Delta G_a^{\neq}$ barriers than with surface methyl in MFI and CHA. In MFI, rate ratios (Eq. (13)) generally exceed 1 for propyl and *sec*-butyl (forming secondary carbocations) at alkyl ratios near 10^{-10} and exceed 1 for ethyl at an alkyl ratio near 10^{-6} in MFI (Fig. 11b), while *tert*-butyl also accelerates rates (rate ratio of unity near 10^{-4}) but less dramatically in this reaction as it forms a bulky C_8 complex which may have some steric repulsions with the MFI framework. However, the alkene-mediated pathway in CHA preferentially occurs via reaction of C_4H_8 with CH_3–Z until substituted alkyl concentrations are near 10^{-3} times that of CH_3–Z (Fig. 11b), while reactions between C_4H_8 and *tert*-butyl occur with very low predicted rates in CHA. Generally, both CH_2O-mediated and alkene-mediated routes proceed through reaction of the donor with secondary or tertiary surface-bound alkyls. Furthermore, MFI tends to require lower CR_3–Z:CH_3–Z ratios for secondary and tertiary routes to become preferred compared to CHA.

The preference of each surface-bound alkyl to react with either CH_3OH or C_4H_8 is dependent on the difference in $\Delta G_a^{\neq}$ for hydride transfer with each reactant, $\Delta\Delta G_a^{\neq}$, (Eq. (14)):

$$\Delta\Delta G_a^{\neq} = \Delta G_a^{\neq}[CH_2O\text{– mediated}] - \Delta G_a^{\neq}[\text{alkene dis.}] \quad (14)$$

For species that form primary (C_1) and secondary carbocations (C_2, C_3, *sec*-C_4), $\Delta\Delta G_a^{\neq}$ is >0 kJ mol^{-1} indicating that the alkene-mediated route is favored (assuming equal pressures of CH_3OH

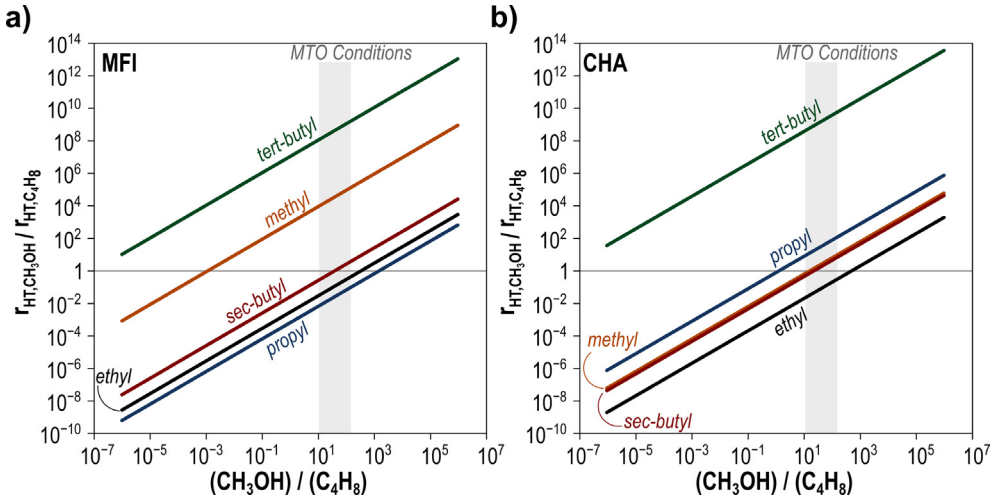

Fig. 12. **a)** Ratio of rate of hydride transfer with CH_3OH to rate of hydride transfer with C_4H_8 for *tert*-butyl (green), *sec*-butyl (red), propyl (blue), ethyl (black), and methyl (orange) versus the ratio of CH_3OH pressure to C_4H_8 pressure at 623 K in MFI. **b)** Ratio of rate of hydride transfer with CH_3OH to rate of hydride transfer with C_4H_8 for *tert*-butyl (green), *sec*-butyl (red), propyl (blue), ethyl (black), and methyl (orange) versus the ratio of CH_3OH pressure to C_4H_8 pressure at 623 K in CHA. A range of "typical" MTO pressure rations is marked with gray shading. (For interpretation of the references to colour in this figure legend, the reader is referred to the web version of this article.)

and C_4H_8). However, $\Delta\Delta G_a^{\neq}$ is largely negative for *tert*-butyl in MFI ($\Delta\Delta G_a^{\neq}$ of − 101, Table S1) and CHA ($\Delta\Delta G_a^{\neq}$ −89, Table S1), indicating that tertiary alkyls (*tert*-butyl) are much better hydride acceptors when the donor is small (CH_3OH) instead of large (C_4H_8). Direct comparisons of $\Delta\Delta G_a^{\neq}$ assume that the CH_3OH:C_4H_8 pressures are equal; however, at MTO conditions the CH_3OH:C_4H_8 pressure ratio is closer to 10^2 [9,29,52,59,101–103]. We can again use a rate ratio, comparing the CH_2O-mediated and alkene-mediated routes to incorporate pressure differences, given by:

$$\frac{r_{HT,CH_3OH}}{r_{HT,C_4H_8}} = \frac{k'_{HT,CR_3}K_{CH_3OH}(CH_3OH)}{k_{HT,CR_3}K_{C_4H_8}(C_4H_8)} = e^{\frac{-\Delta\Delta G_a^{\neq}}{RT}}\frac{(CH_3OH)}{(C_4H_8)} \quad (15)$$

where (CH_3OH) and (C_4H_8) represent their pressures, k'_{HT,CR_3} represents the hydride transfer between CR_3 and CH_3OH, k_{HT,CR_3} represents the hydride transfer between CR_3 and C_4H_8, and K_{CH_3OH} and $K_{C_4H_8}$ represent adsorption of CH_3OH and C_4H_8 near an alkyl, respectively (Scheme 3). As such, these rate ratios depend on $\Delta\Delta G_a^{\neq}$ and the CH_3OH:C_4H_8 pressure ratio. These rate ratios give insight to which species a surface-bound alkyl will preferentially react with. In MFI and CHA, *tert*-butyl will preferentially react with CH_3OH at CH_3OH:C_4H_8 ratios $>10^{-8}$, i.e., at all meaningful MTO conditions (Fig. 12). Primary and secondary species do not show as strong of a preference to react via CH_2O-mediated routes at MTO conditions. Surface methyls show a strong preference to react with CH_3OH in MFI, with rate ratios exceeding 1 at CH_3OH:C_4H_8 ratios $>10^{-3}$ (Fig. 12a), but the preference is much weaker in CHA as the rate ratio and the CH_3OH:C_4H_8 ratio are nearly equal (Fig. 12b). Weak preferences are also observed for ethyl, propyl, and *sec*-butyl alkyls, again indicating that the rate ratios for the two competing hydride transfer routes examined is largely governed by the CH_3OH:C_4H_8 ratio. Generally, *tert*-butyl shows a strong preference to react via CH_2O-mediated routes and will do so even at low pressures of C_4H_8; however, the preferred route of other species is governed CH_3OH:C_4H_8 ratios, which are typically high during MTO conditions. C_4H_8 is used here as a representative alkene that can form a conjugated diene product, and if other alkenes are present at large concentrations and similarly can undergo hydride transfer reactions with surface alkyls then these alkene-mediated routes may become more relevant. These results support previous experimental work in H-ZSM-5 examining the rates of hydrogen transfer product formation in pure pentene co-feeds (0.004 bar 1-pentene) with methanol-mixed co-feeds (0.1 bar CH_3OH and 0.004 bar 1-pentene), which demonstrate that methanol-mixed co-feeds increase hydrogen transfer product yield by ~4-times [52].

4. Conclusions

Diene formation via alkene-mediated and CH_2O-mediated routes is investigated in MFI and CHA zeolites. Alkene-mediated pathways preferentially occur via a sequential mechanism, as opposed to concerted, where ethene first forms C_2H_5–Z and subsequently reacts with butene to form butadiene, occurring with $\Delta G^{\neq}$ of 88 kJ mol^{-1} in MFI and 75 kJ mol^{-1} in CHA. Similarly, CH_2O-mediated routes occur with the lowest effective barriers when CH_3OH adsorbs and reacts to form CH_3–Z, followed by a hydride transfer between CH_3–Z and a second CH_3OH ($\Delta G^{\neq}$ 127 kJ mol^{-1} in MFI and 117 kJ mol^{-1} in CHA). Both routes preferentially occur through the formation of surface alkyls rather than through concerted pathways that bypass zeolite alkylation.

The rate of both routes is governed by the reaction of a surface-bound alkyl with either CH_3OH (CH_2O-mediated) or C_4H_8 (alkene-mediated). As such, both hydride transfer steps were investigated with surface-bound methyl, ethyl, propyl, *sec*-butyl, and *tert*-butyl to determine the effect of size and substitution of different alkyls on hydride transfer barriers and rates. Generally, CH_2O-mediated hydride transfer barriers decrease with increasing alkene substitution, especially in MFI where reaction of CH_3OH with *tert*-butyl occurs with a $\Delta G_a^{\neq}$ (Eq. 12) of 55 kJ mol^{-1} (>40 kJ mol^{-1} lower than all other species). In CHA, the reaction of CH_3OH with *tert*-butyl occurs with the lowest energy $\Delta G_a^{\neq}$ barrier; however, it is not nearly as favorable as MFI—perhaps because steric repulsion begins to play a role in CHA cages before the channels of MFI. Conversely, alkene-mediated routes occur most favorably when a secondary carbocation (propyl in MFI and *sec*-butyl in CHA) reacts with C_4H_8. In both frameworks, the hydride transfer between C_4H_8 and *tert*-butyl has a barrier >40 kJ mol^{-1} higher than all other species, likely because this reaction forms bulky C_8 complexes that are sterically hindered. This preference for larger alkyls to be hydride acceptors indicates that alkene cycle intermediates and products will play a large role in the rate of CH_2O and C_4H_8 formation as the hydrocarbon pool evolves while at startup conditions, even if the concentration of those substituted surface alkyls is very low compared to that of surface methyls.

Comparing the free energy hydride transfer barriers between alkene-mediated and CH_2O-mediated routes for each structure, we find that alkene-mediated pathways are preferred, except for *tert*-butyl where CH_2O-mediated routes are strongly preferred (by over 80 kJ mol^{-1}). However, direct comparisons of free energy hydride transfer barriers are not accurate as the preferred route is highly dependent on CH_3OH:C_4H_8 pressures. Taking the ratio of each route and comparing it to CH_3OH:C_4H_8 pressures ranging from 10^{-6} to 10^6, we find that *tert*-butyl reacts through CH_2O-mediated routes even when the pressure of CH_3OH is 10^6 times lower than C_4H_8 in MFI and 10^4 times lower in CHA. However, the preferred route of primary and secondary carbocations is dependent on the CH_3OH:C_4H_8 pressure ratio. At MTO conditions (CH_3OH:C_4H_8 of 10^2), generally species react via CH_2O-mediated routes; however, at lower ratios, such as 10, species begin to react via alkene-mediated routes.

MTO predominantly produces ethene and propene, but larger alkenes are known to be present and reactive in the olefin cycle. These results suggest that those C_2 and C_3 product alkenes and larger alkenes involved in the alkene cycle can also form surface-bound alkyls that are effective hydride acceptors, thus accelerating the rate of diene formation through direct or indirect (via CH_2O) routes. Given that CH_3OH concentrations are expected to be higher than the concentrations of $C_{\geq 4}$ alkenes required to make conjugated dienes through direct reactions, it seems likely that CH_2O formation rates are higher than those of direct C_4H_6 formation through alkene-mediated reactions, and that these CH_2O intermediates can easily form C_4H_6 through butenol formation followed by dehydration, as suggested in prior reports [48,54]. Our conclusion that CH_2O is likely formed via product-derived surface-bound alkyls instead of the reactant-derived CH_3 MASI is crucial for informing potential strategies to mitigate catalyst deactivation during MTO. Furthermore, it underscores the importance of considering all potential reactants when proposing mechanisms for processes such as MTO that form reactive products.

Declaration of Competing Interest

The authors declare that they have no known competing financial interests or personal relationships that could have appeared to influence the work reported in this paper.

Acknowledgements

This work was funded by an NSF CAREER Award (1942684-CBET). Computational resources were provided by the Extreme

Science and Engineering Discovery Environment and University of Florida Research Computing.

Appendix A. Supplementary data

Supplementary data to this article can be found online at https://doi.org/10.1016/j.jcat.2021.05.010.

References

[1] A. Hwang, A. Bhan, Deactivation of Zeolites and Zeotypes in Methanol-to-Hydrocarbons Catalysis: Mechanisms and Circumvention, Acc. Chem. Res. 52 (9) (2019) 2647–2656, https://doi.org/10.1021/acs.accounts.9b00204.

[2] D. Rojo-Gama, M. Signorile, F. Bonino, S. Bordiga, U. Olsbye, K.P. Lillerud, P. Beato, S. Svelle, Structure–deactivation relationships in zeolites during the methanol–to-hydrocarbons reaction: Complementary assessments of the coke content, J. Catal. 351 (2017) 33–48, https://doi.org/10.1016/j.jcat.2017.04.015.

[3] D. Rojo-Gama, M. Nielsen, D.S. Wragg, M. Dyballa, J. Holzinger, H. Falsig, L.F. Lundegaard, P. Beato, R.Y. Brogaard, K.P. Lillerud, U. Olsbye, S. Svelle, A Straightforward Descriptor for the Deactivation of Zeolite Catalyst H-ZSM-5, ACS Catal. 7 (12) (2017) 8235–8246, https://doi.org/10.1021/acscatal.7b0219310.1021/acscatal.7b02193.s001.

[4] J. Li, Y. Wei, Y. Qi, P. Tian, B. Li, Y. He, F. Chang, X. Sun, Z. Liu, Conversion of methanol over H-ZSM-22: The reaction mechanism and deactivation, Catal. Today 164 (1) (2011) 288–292, https://doi.org/10.1016/j.cattod.2010.10.095.

[5] S. Müller, Y. Liu, M. Vishnuvarthan, X. Sun, A.C. van Veen, G.L. Haller, M. Sanchez-Sanchez, J.A. Lercher, Coke formation and deactivation pathways on H-ZSM-5 in the conversion of methanol to olefins, J. Catal. 325 (2015) 48–59, https://doi.org/10.1016/j.jcat.2015.02.013.

[6] M. Guisnet, L. Costa, F.R. Ribeiro, Prevention of zeolite deactivation by coking, J. Mol. Catal. A: Chem. 305 (1-2) (2009) 69–83, https://doi.org/10.1016/j.molcata.2008.11.012.

[7] M. Dusselier, M.E. Davis, Small-Pore Zeolites: Synthesis and Catalysis, Chem. Rev. 118 (11) (2018) 5265–5329, https://doi.org/10.1021/acs.chemrev.7b00738.

[8] J. Van der Mynsbrugge, A. Janda, L.-C. Lin, V. Van Speybroeck, M. Head-Gordon, A.T. Bell, Understanding Brønsted-Acid Catalyzed Monomolecular Reactions of Alkanes in Zeolite Pores by Combining Insights from Experiment and Theory, ChemPhysChem 19 (4) (2018) 341–358, https://doi.org/10.1002/cphc.201701084.

[9] I.M. Dahl, H. Mostad, D. Akporiaye, R. Wendelbo, Structural and chemical influences on the MTO reaction: a comparison of chabazite and SAPO-34 as MTO catalysts, Micropor. Mesopor. Mater. 29 (1-2) (1999) 185–190, https://doi.org/10.1016/S1387-1811(98)00330-8.

[10] R. Martínez-Franco, Z. Li, J. Martínez-Triguero, M. Moliner, A. Corma, Improving the catalytic performance of SAPO-18 for the methanol-to-olefins (MTO) reaction by controlling the Si distribution and crystal size, Catal. Sci. Technol. 6 (8) (2016) 2796–2806, https://doi.org/10.1039/C5CY02298C.

[11] P. Tian, Y. Wei, M. Ye, Z. Liu, Methanol to olefins (MTO): from fundamentals to commercialization, ACS Catal. 5 (3) (2015) 1922–1938, https://doi.org/10.1021/acscatal.5b00007.

[12] X. Zhao, J. Li, P. Tian, L. Wang, X. Li, S. Lin, X. Guo, Z. Liu, Achieving a super-long lifetime in the zeolite-catalyzed MTO reaction under high pressure: synergistic effect of hydrogen and water, ACS Catal. 9 (4) (2019) 3017–3025, https://doi.org/10.1021/acscatal.8b0440210.1021/acscatal.8b04402.s001.

[13] W. Wu, W. Guo, W. Xiao, M. Luo, Methanol conversion to olefins (MTO) over H-ZSM-5: Evidence of product distribution governed by methanol conversion, Fuel Process. Technol. 108 (2013) 19–24, https://doi.org/10.1016/j.fuproc.2012.05.013.

[14] C.-M. Wang, Y.-D. Wang, H.-X. Liu, G. Yang, Y.-J. Du, Z.-K. Xie, Aromatic-based hydrocarbon pool mechanism for methanol-to-olefins conversion in H-SAPO-18: A van der Waals density functional study, Chin. J. Catal. 36 (9) (2015) 1573–1579, https://doi.org/10.1016/S1872-2067(15)60891-9.

[15] B. Arstad, J.B. Nicholas, J.F. Haw, Theoretical study of the methylbenzene side-chain hydrocarbon pool mechanism in methanol to olefin catalysis, J. Am. Chem. Soc. 126 (9) (2004) 2991–3001, https://doi.org/10.1021/ja035923j.

[16] T.V.W. Janssens, S. Svelle, U. Olsbye, Kinetic modeling of deactivation profiles in the methanol-to-hydrocarbons (MTH) reaction: A combined autocatalytic–hydrocarbon pool approach, J. Catal. 308 (2013) 122–130, https://doi.org/10.1016/j.jcat.2013.05.035.

[17] C. Wang, Y. Chu, A. Zheng, J. Xu, Q. Wang, P. Gao, et al., New insight into the hydrocarbon-pool chemistry of the methanol-to-olefins conversion over zeolite H-ZSM-5 from GC-MS, solid-state NMR spectroscopy, and DFT calculations, Chem. Eur. J. 20 (2014) 12432–12443, https://doi.org/10.1002/chem.201403972.

[18] K. Hemelsoet, J. Van der Mynsbrugge, K. De Wispelaere, M. Waroquier, V. Van Speybroeck, Unraveling the reaction mechanisms governing methanol-to-olefins catalysis by theory and experiment, ChemPhysChem 14 (8) (2013) 1526–1545, https://doi.org/10.1002/cphc.v14.810.1002/cphc.201201023.

[19] P. Bollini, A. Bhan, Improving HSAPO-34 Methanol-to-Olefin Turnover Capacity by Seeding the Hydrocarbon Pool, ChemPhysChem 19 (4) (2018) 479–483, https://doi.org/10.1002/cphc.201701027.

[20] M. Seiler, W. Wang, A. Buchholz, M. Hunger, Direct evidence for a catalytically active role of the hydrocarbon pool formed on zeolite H-ZSM-5 during the methanol-to-olefin conversion, Catal. Lett. 88 (2003) 187–191.

[21] S. Wang, Y. Chen, Z. Qin, T.-S. Zhao, S. Fan, M. Dong, J. Li, W. Fan, J. Wang, Origin and evolution of the initial hydrocarbon pool intermediates in the transition period for the conversion of methanol to olefins over H-ZSM-5 zeolite, J. Catal. 369 (2019) 382–395, https://doi.org/10.1016/j.jcat.2018.11.018.

[22] C. Wang, J. Xu, G. Qi, Y. Gong, W. Wang, P. Gao, Q. Wang, N. Feng, X. Liu, F. Deng, Methylbenzene hydrocarbon pool in methanol-to-olefins conversion over zeolite H-ZSM-5, J. Catal. 332 (2015) 127–137, https://doi.org/10.1016/j.jcat.2015.10.001.

[23] K. Lee, S.B. Hong, Hydrocarbon Pool Mechanism of the Zeolite-Catalyzed Conversion of Ethene to Propene, ACS Catal. 9 (12) (2019) 10640–10648, https://doi.org/10.1021/acscatal.9b0343410.1021/acscatal.9b03434.s001.

[24] A. Hwang, D. Prieto-Centurion, A. Bhan, Isotopic tracer studies of methanol-to-olefins conversion over HSAPO-34: The role of the olefins-based catalytic cycle, J. Catal. 337 (2016) 52–56, https://doi.org/10.1016/j.jcat.2016.01.021.

[25] R. Johansson, S.L. Hruby, J. Rass-Hansen, C.H. Christensen, The Hydrocarbon Pool in Ethanol-to-Gasoline over HZSM-5 Catalysts, Catal. Lett. 127 (1-2) (2009) 1–6, https://doi.org/10.1007/s10562-008-9711-2.

[26] C.-M. Wang, Y.-D. Wang, Z.-K. Xie, Insights into the reaction mechanism of methanol-to-olefins conversion in HSAPO-34 from first principles: Are olefins themselves the dominating hydrocarbon pool species?, J. Catal. 301 (2013) 8–19, https://doi.org/10.1016/j.jcat.2013.01.024.

[27] P. Dejaifve, J.C. Védrine, V. Bolis, E. Derouane, Reaction pathways for the conversion of methanol and olefins on H-ZSM-5 zeolite, J. Catal. 63 (1980) 331–345, https://doi.org/10.1016/0021-9517(80)90086-X.

[28] S. Wang, Y. Chen, Z. Wei, Z. Qin, H. Ma, M. Dong, J. Li, W. Fan, J. Wang, Polymethylbenzene or Alkene Cycle? Theoretical Study on Their Contribution to the Process of Methanol to Olefins over H-ZSM-5 Zeolite, J. Phys. Chem. C 119 (51) (2015) 28482–28498.

[29] X. Sun, S. Mueller, H. Shi, G.L. Haller, M. Sanchez-Sanchez, A.C. van Veen, J.A. Lercher, On the impact of co-feeding aromatics and olefins for the methanol-to-olefins reaction on HZSM-5, J. Catal. 314 (2014) 21–31, https://doi.org/10.1016/j.jcat.2014.03.013.

[30] C.-M. Wang, Y.-D. Wang, Z.-K. Xie, Verification of the dual cycle mechanism for methanol-to-olefin conversion in HSAPO-34: a methylbenzene-based cycle from DFT calculations, Catal. Sci. Technol. 4 (8) (2014) 2631–2638, https://doi.org/10.1039/C4CY00262H.

[31] I.M. Hill, S.A. Hashimi, A. Bhan, Kinetics and mechanism of olefin methylation reactions on zeolites, J. Catal. 285 (1) (2012) 115–123, https://doi.org/10.1016/j.jcat.2011.09.018.

[32] S. Ilias, A. Bhan, Mechanism of the catalytic conversion of methanol to hydrocarbons, ACS Catal. 3 (1) (2013) 18–31, https://doi.org/10.1021/cs3006583.

[33] S. Svelle, F. Joensen, J. Nerlov, U. Olsbye, K.-P. Lillerud, S. Kolboe, et al., Conversion of methanol into hydrocarbons over zeolite H-ZSM-5: ethene formation is mechanistically separated from the formation of higher alkenes, J. Am. Chem. Soc. 128 (2006) 14770–14771, https://doi.org/10.1021/ja065810a.

[34] B. Wilhelmsson, Formaldehyde, Rhinology. 23 (1985) 128–129.

[35] S. Wang, I. Agirrezabal-Telleria, A. Bhan, D. Simonetti, K. Takanabe, E. Iglesia, Catalytic routes to fuels from C1 and oxygenate molecules, Faraday Discuss 197 (2017) 9–39, https://doi.org/10.1039/c7fd00018a.

[36] A. Hwang, M. Kumar, J.D. Rimer, A. Bhan, Implications of methanol disproportionation on catalyst lifetime for methanol-to-olefins conversion by HSSZ-13, J. Catal. 346 (2017) 154–160, https://doi.org/10.1016/j.jcat.2016.12.003.

[37] D.B. Lukyanov, N.S. Gnep, M.R. Guisnet, Kinetic modeling of propane aromatization reaction over HZSM-5 and GaHZSM-5, Ind. Eng. Chem. Res. 34 (2) (1995) 516–523, https://doi.org/10.1021/ie00041a012.

[38] D.B. Lukyanov, N.S. Gnep, M.R. Guisnet, Kinetic modeling of ethene and propene aromatization over HZSM-5 and GaHZSM-5, Ind. Eng. Chem. Res. 33 (2) (1994) 223–234, https://doi.org/10.1021/ie00026a008.

[39] Y.V. Joshi, K.T. Thomson, Brønsted Acid Catalyzed Cyclization of C7 and C8 Dienes in HZSM-5: A Hybrid QM/MM Study and Comparison with C6 Diene Cyclization, J. Phys. Chem. C 112 (33) (2008) 12825–12833, https://doi.org/10.1021/jp712071k.

[40] Y.V. Joshi, A. Bhan, K.T. Thomson, DFT-Based Reaction Pathway Analysis of Hexadiene Cyclization via Carbenium Ion Intermediates: Mechanistic Study of Light Alkane Aromatization Catalysis, J. Phys. Chem. B 108 (2004) 971–980, https://doi.org/10.1021/jp036205m.

[41] Y. Joshi, K. Thomson, Embedded cluster (QM/MM) investigation of C6 diene cyclization in HZSM-5, J. Catal. 230 (2) (2005) 440–463, https://doi.org/10.1016/j.jcat.2004.12.016.

[42] C.-M. Wang, Y.-D. Wang, Z.-K. Xie, Z.-P. Liu, Methanol to Olefin Conversion on HSAPO-34 Zeolite from Periodic Density Functional Theory Calculations: A Complete Cycle of Side Chain Hydrocarbon Pool Mechanism, J. Phys. Chem. C 113 (11) (2009) 4584–4591, https://doi.org/10.1021/jp810350x.

[43] S. Ilias, A. Bhan, The mechanism of aromatic dealkylation in methanol-to-hydrocarbons conversion on H-ZSM-5: What are the aromatic precursors to

light olefins?, J. Catal. 311 (2014) 6–16, https://doi.org/10.1016/j.jcat.2013.11.003.
[44] J.S. Martinez-Espin, M. Mortén, T.V.W. Janssens, S. Svelle, P. Beato, U. Olsbye, New insights into catalyst deactivation and product distribution of zeolites in the methanol-to-hydrocarbons (MTH) reaction with methanol and dimethyl ether feeds, Catal. Sci. Technol. 7 (13) (2017) 2700–2716, https://doi.org/10.1039/C7CY00129K.
[45] W. Dai, G. Wu, L. Li, N. Guan, M. Hunger, Mechanisms of the Deactivation of SAPO-34 Materials with Different Crystal Sizes Applied as MTO Catalysts, ACS Catal. 3 (4) (2013) 588–596, https://doi.org/10.1021/cs400007v.
[46] M. Bjørgen, U. Olsbye, S. Kolboe, Coke precursor formation and zeolite deactivation: mechanistic insights from hexamethylbenzene conversion, J. Catal. 215 (2003) 30–44, https://doi.org/10.1016/S0021-9517(02)00050-7.
[47] M. Bjørgen, S. Akyalcin, U. Olsbye, S. Benard, S. Kolboe, S. Svelle, Methanol to hydrocarbons over large cavity zeolites: Toward a unified description of catalyst deactivation and the reaction mechanism, J. Catal. 275 (1) (2010) 170–180, https://doi.org/10.1016/j.jcat.2010.08.001.
[48] S. Müller, Y. Liu, F.M. Kirchberger, M. Tonigold, M. Sanchez-Sanchez, J.A. Lercher, Hydrogen Transfer Pathways during Zeolite Catalyzed Methanol Conversion to Hydrocarbons, J. Am. Chem. Soc. 138 (49) (2016) 15994–16003, https://doi.org/10.1021/jacs.6b0960510.1021/jacs.6b09605.s001.
[49] J.S. Martínez-Espín, K. De Wispelaere, T.V.W. Janssens, S. Svelle, K.P. Lillerud, P. Beato, V. Van Speybroeck, U. Olsbye, Hydrogen Transfer versus Methylation: On the Genesis of Aromatics Formation in the Methanol-To-Hydrocarbons Reaction over H-ZSM-5, ACS Catal. 7 (9) (2017) 5773–5780, https://doi.org/10.1021/acscatal.7b0164310.1021/acscatal.7b01643.s001.
[50] S. Ilias, A. Bhan, Tuning the selectivity of methanol-to-hydrocarbons conversion on H-ZSM-5 by co-processing olefin or aromatic compounds, J. Catal. 290 (2012) 186–192, https://doi.org/10.1016/j.jcat.2012.03.016.
[51] M. Stöcker, Methanol-to-hydrocarbons: catalytic materials and their behavior, Micropor. Mesopor. Mater. 29 (1-2) (1999) 3–48, https://doi.org/10.1016/S1387-1811(98)00319-9.
[52] X. Sun, S. Mueller, Y. Liu, H. Shi, G.L. Haller, M. Sanchez-Sanchez, A.C. van Veen, J.A. Lercher, On reaction pathways in the conversion of methanol to hydrocarbons on HZSM-5, J. Catal. 317 (2014) 185–197, https://doi.org/10.1016/j.jcat.2014.06.017.
[53] K. De Wispelaere, J.S. Martínez-Espín, M.J. Hoffmann, S. Svelle, U. Olsbye, T. Bligaard, Understanding zeolite-catalyzed benzene methylation reactions by methanol and dimethyl ether at operating conditions from first principle microkinetic modeling and experiments, Catal. Today 312 (2018) 35–43, https://doi.org/10.1016/j.cattod.2018.02.042.
[54] Y. Liu, F.M. Kirchberger, S. Müller, M. Eder, M. Tonigold, M. Sanchez-Sanchez, J.A. Lercher, Critical role of formaldehyde during methanol conversion to hydrocarbons, Nat. Commun. 10 (1) (2019), https://doi.org/10.1038/s41467-019-09449-7.
[55] A. Comas-Vives, M. Valla, C. Copéret, P. Sautet, Cooperativity between Al Sites Promotes Hydrogen Transfer and Carbon-Carbon Bond Formation upon Dimethyl Ether Activation on Alumina, ACS Cent. Sci. 1 (6) (2015) 313–319, https://doi.org/10.1021/acscentsci.5b00226.
[56] L. Kubelková, J. Nováková, P. Jírů, Reaction of Small Amounts of Methanol on Hzsm-5, Hy and Modified Y Zeolites, in: Structure and reactivity of modified zeolites, proceedings of an international conference, Elsevier, 1984, pp. 217–224, doi:10.1016/S0167-2991(09)61157-5.
[57] S.S. Arora, A. Bhan, The critical role of methanol pressure in controlling its transfer dehydrogenation and the corresponding effect on propylene-to-ethylene ratio during methanol-to-hydrocarbons catalysis on H-ZSM-5, J. Catal. 356 (2017) 300–306, https://doi.org/10.1016/j.jcat.2017.10.014.
[58] A. Hwang, A. Bhan, Bifunctional Strategy Coupling Y_2 $_O$3 -Catalyzed Alkanal Decomposition with Methanol-to-Olefins Catalysis for Enhanced Lifetime, ACS Catal. 7 (7) (2017) 4417–4422, https://doi.org/10.1021/acscatal.7b00894.
[59] S.S. Arora, D.L.S. Nieskens, A. Malek, A. Bhan, Lifetime improvement in methanol-to-olefins catalysis over chabazite materials by high-pressure H_2 co-feeds, Nat. Catal. 1 (9) (2018) 666–672, https://doi.org/10.1038/s41929-018-0125-2.
[60] S.S. Arora, Z. Shi, A. Bhan, A mechanistic basis for effects of high-pressure H_2 co-feeds on methanol-to-hydrocarbons catalysis over zeolites, ACS Catal. 9 (7) (2019) 6407–6414, https://doi.org/10.1021/acscatal.9b00969.
[61] Z. Shi, M. Neurock, A. Bhan, Methanol-to-Olefins Catalysis on HSSZ-13 and HSAPO-34 and Its Relationship to Acid Strength, ACS Catal. 11 (3) (2021) 1222–1232, https://doi.org/10.1021/acscatal.0c0401110.1021/acscatal.0c04011.s001.
[62] M. DeLuca, C. Janes, D. Hibbitts, Contrasting Arene, Alkene, Diene, and Formaldehyde Hydrogenation in H-ZSM-5, H-SSZ-13, and H-SAPO-34 Frameworks during MTO, ACS Catal. 10 (8) (2020) 4593–4607, https://doi.org/10.1021/acscatal.9b0452910.
[63] G. Kresse, J. Hafner, *Ab initio* molecular dynamics for liquid metals, Phys. Rev. B. 47 (1) (1993) 558–561, https://doi.org/10.1103/PhysRevB.47.558.
[64] G. Kresse, J. Hafner, *Ab initio* molecular-dynamics simulation of the liquid-metal–amorphous-semiconductor transition in germanium, Phys. Rev. B. 49 (20) (1994) 14251–14269, https://doi.org/10.1103/PhysRevB.49.14251.
[65] G. Kresse, J. Furthmüller, Efficient iterative schemes for *ab initio* total-energy calculations using a plane-wave basis set, Phys. Rev. B. 54 (16) (1996) 11169–11186, https://doi.org/10.1103/PhysRevB.54.11169.
[66] G. Kresse, J. Furthmüller, Efficiency of ab-initio total energy calculations for metals and semiconductors using a plane-wave basis set, Comp. Mater. Sci. 6 (1) (1996) 15–50, https://doi.org/10.1016/0927-0256(96)00008-0.
[67] P. Kravchenko, C. Plaisance, D. Hibbitts, A new computational interface for catalysis, Published as pre-print on https://chemrxiv.org/articles/preprint/8040737 (2019). doi:10.26434/chemrxiv.8040737.v3.
[68] J.P. Perdew, K. Burke, M. Ernzerhof, Generalized gradient approximation made simple, Phys. Rev. Lett. 77 (18) (1996) 3865–3868, https://doi.org/10.1103/PhysRevLett.77.3865.
[69] Y. Zhang, W. Yang, Comment on "Generalized gradient approximation made simple, Phys. Rev. Lett. 80 (4) (1998), https://doi.org/10.1103/PhysRevLett.80.890.
[70] B. Hammer, L.B. Hansen, J.K. Nørskov, Improved adsorption energetics within density-functional theory using revised Perdew-Burke-Ernzerhof functionals, Phys. Rev. B. 59 (11) (1999) 7413–7421, https://doi.org/10.1103/PhysRevB.59.7413.
[71] S. Grimme, S. Ehrlich, L. Goerigk, Effect of the damping function in dispersion corrected density functional theory, J. Comput. Chem. 32 (7) (2011) 1456–1465, https://doi.org/10.1002/jcc.v32.710.1002/jcc.21759.
[72] H. Schröder, A. Creon, T. Schwabe, Reformulation of the D3(Becke-Johnson) Dispersion Correction without Resorting to Higher than C_6 Dispersion Coefficients, J. Chem. Theory Comput. 11 (2015) 3163–3170, https://doi.org/10.1021/acs.jctc.5b00400.
[73] S. Grimme, J. Antony, S. Ehrlich, H. Krieg, A consistent and accurate ab initio parametrization of density functional dispersion correction (DFT-D) for the 94 elements H-Pu, J. Chem. Phys. 132 (15) (2010) 154104, https://doi.org/10.1063/1.3382344.
[74] H.J. Monkhorst, J.D. Pack, Special points for Brillouin-zone integrations, Phys. Rev. B. 13 (12) (1976) 5188–5192, https://doi.org/10.1103/PhysRevB.13.5188.
[75] A. Hoffman, M. DeLuca, D. Hibbitts, Restructuring of MFI framework zeolite models and their associated artifacts in density functional theory calculations, J. Phys. Chem. C 123 (11) (2019) 6572–6585, https://doi.org/10.1021/acs.jpcc.8b1223010.
[76] C. Baerlocher, L.B. McCusker, Database of Zeolite Structures, 2013: http://www.iza-structure.org/databases (accessed January 5, 2017).
[77] A. Ghorbanpour, J.D. Rimer, L.C. Grabow, Computational Assessment of the Dominant Factors Governing the Mechanism of Methanol Dehydration over H-ZSM-5 with Heterogeneous Aluminum Distribution, ACS Catal. 6 (4) (2016) 2287–2298, https://doi.org/10.1021/acscatal.5b0236710.1021/acscatal.5b02367.s001.
[78] C.T. Nimlos, A.J. Hoffman, Y.G. Hur, B.J. Lee, J.R. Di Iorio, D.D. Hibbitts, R. Gounder, Experimental and Theoretical Assessments of Aluminum Proximity in MFI Zeolites and Its Alteration by Organic and Inorganic Structure-Directing Agents, Chem. Mater. 32 (21) (2020) 9277–9298, https://doi.org/10.1021/acs.chemmater.0c0315410.1021/acs.chemmater.0c03154.s001.
[79] M. DeLuca, P. Kravchenko, A. Hoffman, D. Hibbitts, Mechanism and Kinetics of Methylating C6–C12 Methylbenzenes with Methanol and Dimethyl Ether in H-MFI Zeolites, ACS Catal. 9 (7) (2019) 6444–6460, https://doi.org/10.1021/acscatal.9b00650.
[80] A.J. Jones, E. Iglesia, The strength of Brønsted acid sites in microporous aluminosilicates, ACS Catal. 5 (10) (2015) 5741–5755, https://doi.org/10.1021/acscatal.5b01133.
[81] S. Nystrom, A. Hoffman, D. Hibbitts, Tuning Brønsted acid strength by altering site proximity in CHA framework zeolites, ACS Catal. 8 (9) (2018) 7842–7860, https://doi.org/10.1021/acscatal.8b02049.
[82] H. Jónsson, G. Mills, K.W. Jacobsen, Nudged elastic band method for finding minimum energy paths of transitions, in: B.J. Berne, G. Ciccotti, D.F. Coker (Eds.), Classical and Quantum Dynamics in Condensed Phase Simulations, World Scientific, 1998, pp. 385–404, https://doi.org/10.1142/9789812839664_0016.
[83] G. Henkelman, H. Jónsson, A dimer method for finding saddle points on high dimensional potential surfaces using only first derivatives, J. Chem. Phys. 111 (15) (1999) 7010–7022, https://doi.org/10.1063/1.480097.
[84] J.S. Martinez-Espin, K. De Wispelaere, M. Westgård Erichsen, S. Svelle, T.V.W. Janssens, V. Van Speybroeck, P. Beato, U. Olsbye, Van Speybroeck, et al., Benzene co-reaction with methanol and dimethyl ether over zeolite and zeotype catalysts: Evidence of parallel reaction paths to toluene and diphenylmethane, J. Catal. 349 (2017) 136–148, https://doi.org/10.1016/j.jcat.2017.03.007.
[85] P.N. Plessow, F. Studt, How accurately do approximate density functionals predict trends in acidic zeolite catalysis?, J. Phys. Chem. Lett. 11 (11) (2020) 4305–4310, https://doi.org/10.1021/acs.jpclett.0c0124010.1021/acs.jpclett.0c01240.s001.
[86] M.L. Sarazen, E. Iglesia, Stability of bound species during alkene reactions on solid acids, PNAS 114 (20) (2017) E3900–E3908, https://doi.org/10.1073/pnas.1619557114.
[87] M. Boronat, P. Viruela, A. Corma, A Theoretical Study of the Mechanism of the Hydride Transfer Reaction between Alkanes and Alkenes Catalyzed by an Acidic Zeolite, J. Phys. Chem. A 102 (48) (1998) 9863–9868, https://doi.org/10.1021/jp981484c.
[88] M.J. Janik, R.J. Davis, M. Neurock, A density functional theory study of the alkylation of isobutane with butene over phosphotungstic acid, J. Catal. 244 (1) (2006) 65–77, https://doi.org/10.1016/j.jcat.2006.08.013.
[89] G.M. Mullen, M.J. Janik, Density Functional Theory Study of Alkane-Alkoxide Hydride Transfer in Zeolites, ACS Catal. 1 (2) (2011) 105–115, https://doi.org/10.1021/cs1000619.
[90] M.L. Sarazen, E. Doskocil, E. Iglesia, Effects of void environment and acid strength on alkene oligomerization selectivity, ACS Catal. 6 (10) (2016) 7059–

7070, https://doi.org/10.1021/acscatal.6b0212810.1021/acscatal.6b02128.s001.
[91] A.J. Jones, E. Iglesia, Kinetic, spectroscopic, and theoretical assessment of associative and dissociative methanol dehydration routes in zeolites, Angew. Chem. Int. Ed. Engl. 53 (45) (2014) 12177–12181, https://doi.org/10.1002/anie.201406823.
[92] J.R. Di Iorio, A.J. Hoffman, C.T. Nimlos, S. Nystrom, D. Hibbitts, R. Gounder, Mechanistic origins of the high-pressure inhibition of methanol dehydration rates in small-pore acidic zeolites, J. Catal. 380 (2019) 161–177, https://doi.org/10.1016/j.jcat.2019.10.012.
[93] D. Masih, S. Rohani, J.N. Kondo, T. Tatsumi, Low-temperature methanol dehydration to dimethyl ether over various small-pore zeolites, Appl. Catal. B 217 (2017) 247–255, https://doi.org/10.1016/j.apcatb.2017.05.089.
[94] W. Song, D.M. Marcus, H. Fu, J.O. Ehresmann, J.F. Haw, An oft-studied reaction that may never have been: direct catalytic conversion of methanol or dimethyl ether to hydrocarbons on the solid acids HZSM-5 or HSAPO-34, J. Am. Chem. Soc. 124 (2002) 3844–3845, https://doi.org/10.1021/ja016499u.
[95] P.N. Plessow, F. Studt, Theoretical Insights into the Effect of the Framework on the Initiation Mechanism of the MTO Process, Catal. Lett. 148 (4) (2018) 1246–1253, https://doi.org/10.1007/s10562-018-2330-7.
[96] M.L. Sarazen, E. Doskocil, E. Iglesia, Catalysis on solid acids: Mechanism and catalyst descriptors in oligomerization reactions of light alkenes, J. Catal. 344 (2016) 553–569, https://doi.org/10.1016/j.jcat.2016.10.010.
[97] R. Gounder, E. Iglesia, The roles of entropy and enthalpy in stabilizing ion-pairs at transition states in zeolite acid catalysis, Acc. Chem. Res. 45 (2) (2012) 229–238, https://doi.org/10.1021/ar200138n.
[98] A.J. Jones, S.I. Zones, E. Iglesia, Implications of Transition State Confinement within Small Voids for Acid Catalysis, J. Phys. Chem. C 118 (31) (2014) 17787–17800, https://doi.org/10.1021/jp5050095.
[99] M.L. Sarazen, E. Iglesia, Effects of charge, size, and shape of transition states, bound intermediates, and confining voids in reactions of alkenes on solid acids, ChemCatChem 10 (18) (2018) 4028–4037, https://doi.org/10.1002/cctc.v10.1810.1002/cctc.201800401.
[100] X. Wu, S. Xu, Y. Wei, W. Zhang, J. Huang, S. Xu, Y. He, S. Lin, T. Sun, Z. Liu, Evolution of C-C Bond Formation in the Methanol-to-Olefins Process: From Direct Coupling to Autocatalysis, ACS Catal. 8 (8) (2018) 7356–7361, https://doi.org/10.1021/acscatal.8b0238510.1021/acscatal.8b02385.s001.
[101] M. Bjorgen, S. Svelle, F. Joensen, J. Nerlov, S. Kolboe, F. Bonino, L. Palumbo, S. Bordiga, U. Olsbye, Conversion of methanol to hydrocarbons over zeolite H-ZSM-5: On the origin of the olefinic species, J. Catal. 249 (2) (2007) 195–207, https://doi.org/10.1016/j.jcat.2007.04.006.
[102] F.L. Bleken, S. Chavan, U. Olsbye, M. Boltz, F. Ocampo, B. Louis, Conversion of methanol into light olefins over ZSM-5 zeolite: Strategy to enhance propene selectivity, Appl. Catal. A 447–448 (2012) 178–185, https://doi.org/10.1016/j.apcata.2012.09.025.
[103] M. Zhang, S. Xu, Y. Wei, J. Li, J. Wang, W. Zhang, S. Gao, Z. Liu, Changing the balance of the MTO reaction dual-cycle mechanism: Reactions over ZSM-5 with varying contact times, Chin. J. Catal. 37 (8) (2016) 1413–1422, https://doi.org/10.1016/S1872-2067(16)62466-X.